The Pennsylvania State University
The Graduate School
College of Engineering

WIDE-ANGLE OPTICS FOR FULL-DAY OPERATION OF A PLANAR SOLAR CONCENTRATOR EMPLOYING HIGH EFFICIENCY MICROCELL PHOTOVOLTAICS

A Thesis in
Electrical Engineering
by
Jared S. Price

Submitted in Partial Fulfillment
of the Requirements
for the Degree of

Master of Science

December 2014

The thesis of Jared S. Price was reviewed and approved* by the following:

Noel C. Giebink
Assistant Professor of Electrical Engineering

Thomas N. Jackson
Robert E. Kirby Chair Professor of Electrical Engineering

Kultegin Aydin
Professor of Electrical Engineering, Head of Department

*Signatures are on file in the Graduate School.

Abstract

Concentrating photovoltaics (CPV) offer a route to lowering the cost of solar power, but the existing paradigm based on precise orientation of large-area concentrator modules toward the sun limits CPV deployment to large, open land areas. Here, we explore an alternate approach using high efficiency microcell photovoltaics embedded between a pair of plastic lenslet arrays to demonstrate quasi-static CPV panels <1 cm thick that accomplish full-day tracking through small (<1 cm) lateral translation at fixed latitude tilt. Using both commercial off-the-shelf optics and 3D printed lenslet arrays, we validate this approach through direct outdoor testing and show that it enables flux concentration >200x with >70% optical efficiency over a 120° field of view that is sufficient for year-round operation. Per unit of installed land area, cosine projection loss for fixed microtracking CPV panels is ultimately offset by improved ground coverage relative to their conventional dual-axis counterparts, enabling a 1.9x increase in daily energy output that may open up a new opportunity for compact, high-efficiency CPV in rooftop installations and other limited-space urban environments.

Table of Contents

List of Figures

List of Tables

Acknowledgments

I am incredibly grateful for the patience and guidance of my advisor, Dr. Chris Giebink. Thanks to his encouragement, I am finishing out one degree, and I look forward to completing my PhD under his tutelage. I would also like to thank my device physics professor and co-chair, Dr. Tom Jackson, for reinforcing my first responsibility as a student and future scientist - to think. Without the hard work from these two men and a number of other professors and mentors, I would be a considerably more ignorant man.

During my time in graduate school, I have befriended variety of people and strengthened friendships that were already in existence. In particular, I would like to express my gratitude to Tim Eisenhardt and Sarah Yoder for helping proof-read this document and pointing out grammatical errors, as well as concepts that were not clear. I would also like to thank all of my lab mates; without their assistance and suggestions, many of the figures in this document would not look as nice. More importantly, they have put up with me on a daily basis for the last two years, and for that, I am enormously appreciative!

Finally, I would never have made it this far in life without the constant support from my parents, Tim Price and Sherry Hildreth, my sister, Meghan Price and my extended family. I am forever indebted to all of you!

Dedication

I dedicate my master's dissertation work to my grandfather, William Price who has served as an outstanding role model for the entirety of my life, and my late cousin, Jason Liming who was like a brother to me.

Chapter 1
Background and Introduction

Here, we provide basic motivation for renewable energy. Historical data is supplemented with several different scenarios to give an idea of how carbon emissions and energy use may vary in the coming years. An introduction to power generation via photovoltaics (PVs) is provided along with further details about increasing the efficiency of PVs through the concentration of light. After a brief review of modern concentrating photovoltaics (CPV), we conclude this chapter with the basic working principles of our planar solar concentrator design.

1.1 Incentives for Renewable Energy Sources

Among society's most daunting technical challenges in the coming years is that of exchanging our present energy production scheme based on fossil fuels with those derived from clean, sustainable sources. Given that the world's population is projected to reach ∼9.5 billion by 2050, [1] meeting the increased global energy demand in a tenable manner will require both increased efficiency from existing fossil fuel-based sources as well as considerable supplementation from carbon-neutral sources.

A number of different scenarios for climate change research and assessment exist, [2–4] and the most recent Intergovernmental Panel on Climate Change (IPCC) Assessment Report (AR5) uses representative concentration pathways (RCPs), which are the third generation of such scenarios. [5] To get a better handle on energy use, Table 1.1 demonstrates the global energy perspective in terms of total energy consumption, population, GDP, and carbon emissions as projected from 2005 through the remainder of the century using RCP 4.5. [6] This is a moderately aggressive scenario in terms of adopting carbon-neutral energy sources and energy savings and should limit the global temperature increase to ∼2°C by 2100. The global population, N, was ∼6.43 billion people in 2005, and is projected to peak around 9 billion by 2050, after which it decreases through the duration of the simulation. The globally averaged gross domestic product (GDP) per person in 2005 was ∼$6,400 and assuming a historical average rate of increase at 1.4% yr^{-1}, is

Table 1.1. World energy statistics and projections. Values from 2005 are historical data whereas 2035, 2050 and 2095 are from RCP4.5, [6] while estimated values for 2011 are included for comparison. The equivalent carbon emission rate was converted from the CO_2 emission rate by multiplying by the ratio of molecular weights of C to CO_2 (12/44).

Quantity	**Definition**	**Units**	**2005**	**2011**	**2035**	**2050**	**2095**
N	Population	B Persons	6.43	6.94 [7]	8.34	8.81	8.75
GDP	GDP	T$/yr	41.0	71.4 [8]	87.7	123.2	324.0
GDP/N	Per capita GDP	$/(person-yr)	6,368	10,291	14,367	17,698	33,085
$\dot{E}/GDP$	Energy intensity	W/($/yr)	0.35	0.24	0.25	0.20	0.10
$\dot{E}$	Energy consumption rate	TW	14.5	17.4 [9]	22.3	24.9	31.1
$C\dot{O}_2$	Equivalent CO_2 emission rate	$GTCO_2$/yr	32.8	31.3 [10]	42.6	41.4	15.5
$\dot{C}$	Equivalent carbon emission rate	GtC/yr	8.96	8.54	11.61	11.28	4.23
C/E	Carbon intensity	KgC/(W·yr)	0.62	0.49	0.52	0.45	0.14

forecasted to be ∼$17,700 by 2050. Despite any uncertainties in population growth, the increase in GDP/N is potentially low granted the burgeoning economies in developing nations such as China and India; given the rise in both global population and economic development, the energy intensity (energy consumed per unit of GDP, $\dot{E}/GDP$) will also rise. However, because of expected refinements in the production, distribution, and consumption of power, energy intensity is expected to decrease by about 0.8% yr^{-1} as it has over the last century, leading to a change from 0.35 W/($ yr^{-1}) in 2005 to 0.20 W/($ yr^{-1}) in 2050. Although this decrease helps to mitigate increases in population and per capita GDP, energy use is still expected to grow, leading to a world power consumption of 24.9 TW in 2050, which is nearly double the 14.5 TW consumed in 2005. Finally, anthropogenic CO_2 emissions are projected to peak near 42 $GtCO_2$/yr around the year 2040, after which they decline until the year 2080 before leveling off around 15 $GtCO_2$/yr for the remainder of the century.

If we consider all potential fossil fuel reserves and assume consumption similar to 1998 rates, it is estimated that present fossil fuel energy resources could sustain a 25-30 TW global energy consumption rate for several centuries. [11] While human energy demand can be sated purely by fossil fuels, doing so would release epochal amounts of CO_2 into the atmosphere; given that there are no natural destruction mechanisms for CO_2 (i.e. it is only removed via chemical reactions, such as photosynthesis) long-term removal of CO_2 occurs by convection between the atmosphere, the ocean, and the biosphere. To this end, atmospheric CO_2

equilibrates with the near-surface layer of the ocean on a 10-30 year timescale [12], and mixing time between the near-surface and deep ocean layers ranges from 400 to several thousand years. [12, 13] This means that any environmental effects induced by the release of excess CO2 into the atmosphere from anthropogenic sources will likely remain for at least the next 400-2000 years. Even if we cannot say with 100% certainty that CO_2 is linked to climate change, there are still strong indicators that it has played a key role in the earth's climatological cycle. Without any intervention, it is highly probable that global warming will occur, potentially with a positive feedback loop as permafrost melts, both releasing more CO_2 into the atmosphere and decreasing the albedo of the earth's surface. Additional adverse effects of increased atmospheric CO_2 include rising sea levels, changes to the hydrological cycle, and extreme loss in biodiversity, among others. [14]

The International Energy Agency (IEA) releases an annual report describing tabulated estimates for energy consumption. [9, 15] Key results from the two most recent reports showing historical consumption rates as well as an outlook based on relevant scenarios are seen in Figure 1.1. Comparing Figure 1.1a and Figure 1.1b (1973 and 2011, respectively), we can see a $\sim$5% rise in the use of nuclear and renewable energy sources; however, this is over the course of nearly 40 years. In order to keep global temperatures from rising much more than 2 °C as in RPC 4.5, the IPCC recommends that we (the world) keep total atmospheric CO_2 concentrations below 450 ppm. [14] Figure 1.1c presents an optimistic 2035 outlook on global energy consumption assuming that we follow a climate-policy framework aimed at stabilizing global concentrations of equivalent CO_2 emissions, and Figure 1.1d shows what would be required to limit atmospheric CO_2 to 450 ppm. Both scenarios require more than double our global ramp-up rate of carbon-neutral energy sources.

There are three general ways to reduce CO_2 emissions while maintaining or even scaling our energy consumption. The first involves aggressive carbon capture and storage, where CO_2 is dissolved in underground aquifers, or pumped into old oil wells. [16] For this method to work, injected CO_2 must not leak at a rate faster than a globally averaged rate of 1% over several centuries. The global reservoir capacity is estimated to allow for 100 - 150 years of sequestration, but because of the geological variation from reservoir to reservoir, each would have to be tested individually. Furthermore, we must know with >99% confidence that the leak rate will remain below acceptable limits through the foreseeable future. This necessitates large scale modeling, simulation, monitoring, and validation of potential test sites, all of which may take $\sim$10 - 20 years. In the meantime, we must begin to ween ourselves off of fossil fuels and turn to carbon-neutral energy sources.

The second method requires that we consume more nuclear-generated power. [17, 18] Global estimates of U resources are sufficient to provide $\sim$100 TW-yr of electricity using conventional once-through U fission reactor technology. If roughly 1/3 of the world's 2050 energy demand ($\sim$10 TW) were to come from nuclear

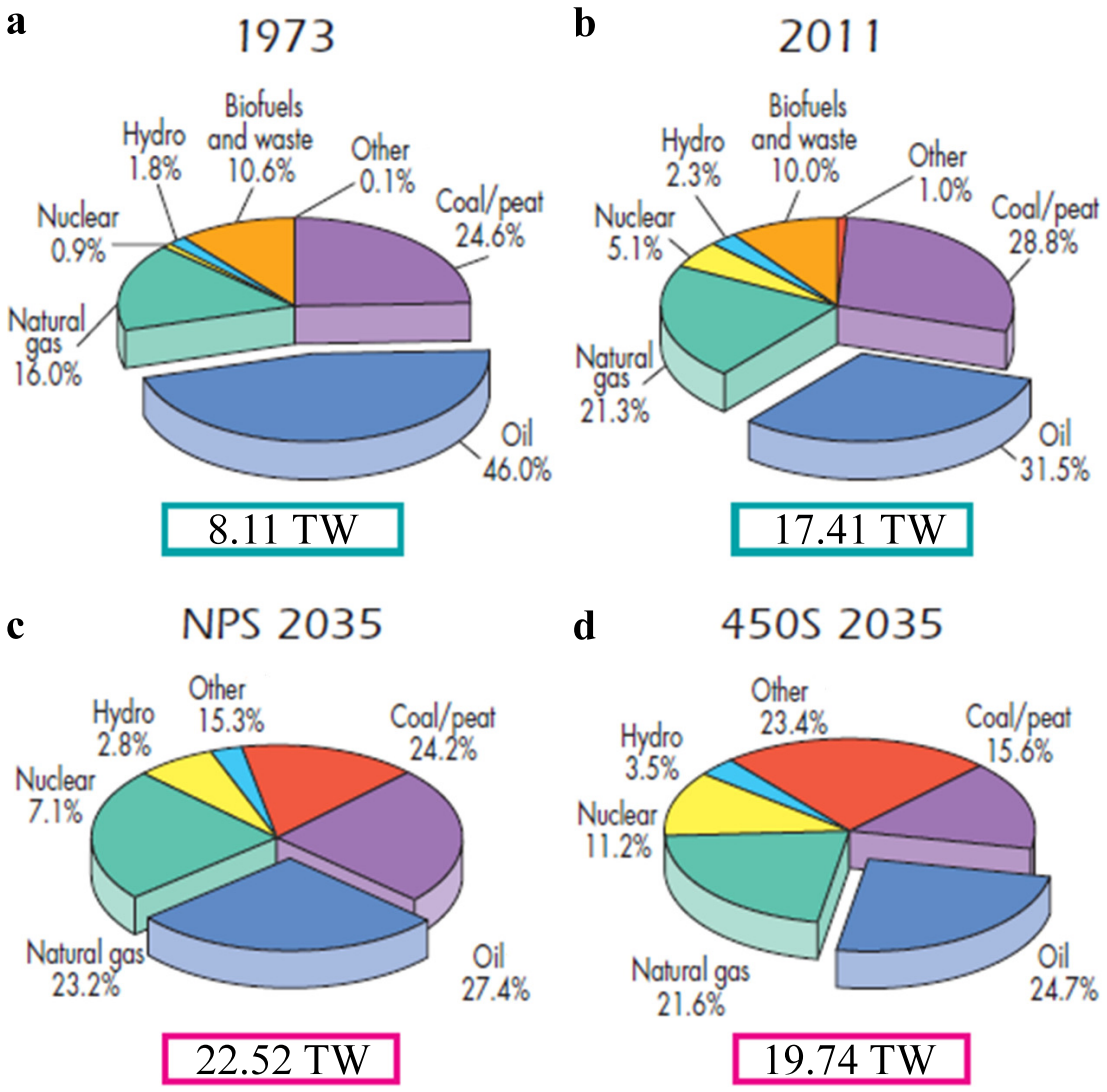

Figure 1.1. Global energy source blends in (a) 1970, [9] (b) 2011, [9] and projected to 2035 based on (c) announced policy commitments and plans detailed in the New Policies Scenario (NPS), [15] and (d) plausible post-2012 climate-policy framework to stabilize the concentration of global greenhouse gases at 450 ppm CO2-equivalent (450S). [15] Total projected energy use for the given year is boxed below each pie chart. Energy from "other" includes that produced from biofuels and waste, geothermal, solar, wind, tide, etc.

fission, terrestrial supplies of U would be depleted within a decade. Because global energy production from nuclear fission was ∼0.9 TW in 2011, [9] for this scenario to become viable, we would have to construct 10,000 1 GW fission plants at a rate of nearly one plant every 1.4 days for the next 36 years; even then, the U stores would run out before the ramp-up phase was completed. An alternative to nuclear fission is nuclear fusion, which has been heralded as the energy source of the future

since the 1950s. Although the United States National Ignition Facility based out of the Lawrence Livermore National Laboratory recently demonstrated a fusion reaction releasing more energy than was input to the system, [19] major challenges still stand in the way of creating the sustained fusion reactions mandatory for long-term, stable power production. At present rates of progression, nuclear fusion will not become cost-effective until at least the later half of the century. This all but removes it from current schemes to reduce CO_2 emissions in the near-term.

Finally, that leaves us with renewable energy sources such as wind, hydro, geothermal, biomass, and solar (collectively labeled as "other" in Figure 1.1). Actively using all of the potential land areas of wind energy generation would yield ∼2-4 TW, with even more power available off-shore. Knowing that these estimates are based on point-source measurements and the high level of the difficulty inherent to transmitting large quantities of off-shore power, a realistic upper limit is 2 TW, which would require two million state-of-the-art wind turbines operating today. [11] If we were to dam water flow from every river, lake, and stream on the planet, hydroelectrics could provide 4.6 TW. Accounting for the fact that it is not practical to do this, a reasonably attainable value of 1.5 TW has been estimated, with 0.9 TW being economically viable; as of 2011, we were operating with 0.4 TW of the global energy mix contributed via hydroelectics. Another possible source of renewable energy is through geothermal production. In some locations, it is possible to use steam rising from the ground to spin turbines; however, because this is not an option for the vast majority of terrestrial regions, it is necessary to drill as deep as ∼10 km into the earth's crust to generate enough steam to run a turbine. Moreover, the amount of heat that can be sustainably harvested is equivalent to the total geothermal heat flux at the earth's surface (57 mW/m^2), and multiplying by all of the land area, we can gain 11.6 TW. Knowing that the second law of thermodynamics will prevent us from obtaining all of this (especially at lower temperature differentials), we would be only able to extract a maximum of ∼2-3 TW. [20]

Given that biomass, solar thermal, and photovoltaics are directly dependent on the sun for energy production, the remaining sources could arguably be lumped together. Every year, 1.5 x 10^5 TW (∼4000x our projected 2050 power requirement) worth of solar energy impinges on the surface of the earth. In less than one hour, the sun provides more energy than we use in an entire year, and as such, solar energy alone can afford our entire carbon-neutral energy demand. [21] At present, if all rain-fed, cultivatable land (not presently in use for food crops) were used for fast-growing fuel crops, biomass could provide 5 TW. This assumes that no energy is required to cultivate the land or process the fuel and is ultimately limited by photosynthesis' ∼1% efficiency under optimal growing conditions. Both of these stipulations are best-case scenarios, and in fact, it takes approximately the same amount of energy from fossil fuels to grow and convert crops to useful forms of energy as we get from the entire cycle. [11] The final energy resource is the direct

use of solar energy, either through solar thermal or solar photovoltaic. Assuming a low averaged efficiency of 10%, it would take ∼65,000 sq.mi (roughly the size of Arkansas, or the area covered by our nation's highways) to produce 3.3 TW. Scaling this by a factor of 6 globally would yield nearly 2/3 of the total projected 2050 power requirements. Alternatively, covering every U.S. rooftop with 10% efficient panels would only generate 0.25 TW [20]; to meet the goal of 3 TW, we would be required to install ∼500,000 2 kW_{peak} solar panels every day from now until 2050! Even if this were an option, there are the issues of storing large amounts of energy created directly via photovoltaics, both daily and seasonal variations in solar insolation due to the tilt of the earth and atmospheric conditions, and the relatively high cost of solar power when compared W/W to that generated by fossil fuels. Nevertheless, solar power is the only carbon-neutral energy source that stands to release us from our addiction to fossil fuels. In the next section, we aim to address some of the basics of solar power, as well as how to increase its efficiency.

1.2 A Semi-Quantitative Overview of Solar Power

Neglecting biomass as a source of solar power, there are two general classes of solar power generation: solar-thermal and solar-photovoltaic. Here, we discuss and compare the two as well as introduce the fundamental workings of a photovoltaic system. An overview of paths to enhance the efficiency of photovoltaics is provided.

1.2.1 Thermal or Photovoltaic Power Generation?

There are a number of methods for solar thermal power generation, [22] but, solar trough systems are the most ubiquitous. These utilize long line-focusing parabolic silvered mirrors that direct incident solar radiation to a tubular receiver/absorber filled with a heat-transfer fluid (HTF). The HTF is heated as it is piped down along the trough and is eventually used to boil water, which creates steam and spins a turbine. [23] Estimating the net optical efficiency of a clean, second-surface silver mirror at 94% and an ideal Rankine cycle operating at the Carnot limit of 63%, the maximum possible efficiency of a solar thermal system is 59%. If we account for optical losses such as shading, dirt on the surface of the mirror and collector, tracking errors, etc., optical efficiency drops to ∼90%, and with actual thermal efficiencies being closer to ∼42%, a feasible goal is ∼38%. This benchmark has almost been realized by a number of plants in the United States. [24]

Though the efficiency of solar thermal energy generation systems are on par with a typical coal-fired power plant, they remain considerably more expensive than their fossil fuel counterparts as a result of higher maintenence costs and complex tracking systems. Additionally, like a coal-fired power plant, they are essentially relegated to utility-scale generation sites as a result of the high temperature gradients required for efficient thermodynamic cycles. This forces a ∼10% transmission loss on any

power generated at a centralized location. Despite these disadvantages, solar-thermal plants offer the ability to store energy in the form of a superheated working fluid such that they can continue to generate power overnight. This is done at a substantially lower cost than an equivalent battery-, capacitor-, pressurized air-, or water reservoir-based system for a photovoltaic approach.

Solar photovoltaic (PV) energy conversion is a single-step process where incident light (photons) above a certain energy is absorbed by a semiconductor to generate an electron-hole pair that is extracted from the material to create power. There exists a wide variety of semiconductor technologies to exploit this effect, including amorphous, microcrystalline, multicrystalline, or single crystal Si, copper indium gallium selenide (CIGS) or cadmium telluride (CdTe) thin films, small molecule, polymer, or hybrid organic heterojunctions, and high efficiency III-IV and multijunction cells. A list of typical cell efficiencies can be seen in Table 1.2.1

Owing to the fact that we have a mature manufacturing base for Si-based PVs, we will use that system as a baseline. From Table 1.2.1, we see that a single crystal Si cell is around 25% efficient, has an open circuit voltage (V_{OC}) of ∼0.7 V, and a short circuit current of ∼60 mA. This gives a total power output of ∼37 mW, which is far too little to be of use on its own. To increase power output to useful levels, it is commonplace to put a row of individual cells in series, which effectively sums the voltage produced by each cell, and then place these rows in parallel to increase the total current output; this type of arrangement is called a module. As a result of inhomogeneities between the cells, the overall efficiency of a module tends to be lower than that of a model single-cell device; typical module efficiencies for an array of single crystal Si cells are on the order of ∼18%. Fresnel reflections will further reduce the efficiency of a PV panel and are least when the panel is directly normal to the sun. This can be partially accomplished if we implement a low-cost single-axis tracker to follow the change in solar zenith, leading to an optical efficiency (based solely off of reflection losses) of ∼81% and a net system efficiency of 15%. Even with this low efficiency, solar PV's principal advantages over solar thermal (as well as nearly every other source of both renewable and nonrenewable energy) are its ability to scale to almost any power requirement (mW to MW), and its relative lack of requisite infrastructure. With the exception of inverters and potentially a small amount of water for semi-annual cleanings, [26] solar PV does not require large turbines or generators because panels are capable of generating DC current by exposing them to light. All the same, in order for solar PV to become cost-competitive, it is necessary to reduce the number of invested \$/W of electricity. The simplest way to do this is to increase the efficiency of a panel.

Table 1.2. A compilation of standard values for an assortment of semiconductor material systems. [25] Different illumination areas are denoted as total area (t), designated illumination area (da) and apertured area (ap). Values tagged with a * are taken on a per cell basis.

Classification	**Efficiency (%)**	**Area (mm^2)**	**V_{OC} (V)**	**J_{SC} (mA/cm^2)**	**Fill Factor (%)**
Silicon					
Si (crystalline)	25.6 ± 0.5	143.7 (da)	0.740	41.8	82.7
Si (multicrystalline)	20.4 ± 0.5	1.002 (ap)	0.664	38.0	80.9
Si (thin film transfer)	20.1 ± 0.4	242.6 (ap)	0.682	38.14*	77.4
Si (thin film minimodule)	10.5 ± 0.3	94.0 (ap)	0.492*	29.7*	72.1
III-V Cells					
GaAs (thin film)	28.8 ± 0.9	0.9927 (ap)	1.122	29.68*	86.5
GaAs (multicrystalline)	18.4 ± 0.5	4.011 (t)	0.994	23.2	79.7
InP (crystalline)	22.1 ± 0.7	4.02 (t)	0.878	29.5	85.4
Thin film chalcogenide					
CIGS (cell)	20.5 ± 0.6	0.9882 (ap)	0.752	35.3d	77.2
CIGS (minimodule)	18.7 ± 0.6	15.892 (da)	0.701*	35.29*	75.6
CdTe (cell)	19.6 ± 0.4	1.0055 (ap)	0.8573	28.59*	80.0
Amorphous/micro Si					
Si (amorphous)	10.1 ± 0.3	1.036 (ap)	0.886	16.75*	67.8
Si (microcrystalline)	11.0 ± 0.3	1.045 (da)	0.542	27.44*	73.8
Dye sensitised					
Dye sensitised	11.9 ± 0.4	1.005 (da)	0.744	22.47*	71.2
Dye sensitised (minimodule)	29.9 ± 0.4	17.11 (ap)	0.719*	19.4*	71.4
Dye (submodule)	8.8 ± 0.3	398.8 (da)	0.697*	18.42*	68.7
Organic					
Organic (thin film)	10.7 ± 0.3	1.013 (da)	0.872	17.75*	68.9
Organic (minimodule)	9.1 ± 0.3	25.04 (da)	0.794*	17.06*	67.5
Organic (submodule)	6.8 ± 0.2	395.9 (da)	0.798*	13.50*	62.8
Perovskite (thin film)	17.9 ± 0.8	0.0937 (ap)	1.1142	21.8	73.6
Multijunction devices					
InGaP/GaAs/InGaAs	37.9 ± 1.2	1.047 (ap)	3.065	14.27*	86.7
a-Si/nc-Si/nc-Si (thin film)	13.4 ± 0.4	1.006 (ap)	1.963	9.52*	71.9
a-Si/nc-Si (thin film cell)	12.3 ± 0.3	0.962(ap)	1.365	12.93*	69.4
a-Si/nc-Si (thin film minimodule)	11.8 ± 0.6	40.26 (ap)	1.428*	12.27*	67.5

1.2.2 Fundamentals of Photovoltaics

Before we can truly understand how to go about improving the efficiency of a PV unit, it is necessary to review how photocurrent is generated and what the limiting factors are. In 1961, Shockley and Queisser proposed an upper limit on efficiency using a detailed balance. [27] Any body above 0 K will emit blackbody radiation; this is why the sun (∼6000 K) emits light and why heating elements in an oven (∼3000 K) glow red and radiate heat. If we assume a solar cell in equilibrium to be around room temperature, T_a (∼300 K), it will also emit and receive long wavelength infrared radiation from its environment such that these rates are equivalent. This thermal photon flux from the ambient to a flat plate solar cell, $b_a(e)$ is given in Equation 1.1,

$$b_a = \frac{2F_a}{h^3c^2}\left(\frac{E^2}{e^{E/k_BT_a} - 1}\right) \tag{1.1}$$

where F_a is a geometric factor equal to π (radiation is received over a hemisphere), and h, c, and k_B are Planck's constant, the speed of light, and Boltzmann's constant, respectively. Equation 1.2 describes the equivalent current density absorbed from the ambient in the absence of light,

$$J_{abs} = q(1 - R(E))\alpha(E)b_a(E) \tag{1.2}$$

where q is the fundamental unit of charge, $R(E)$ is the probability of photon reflection for a certain photon energy, and $\alpha(E)$ is the absorptivity of the material as determined by the absorption coefficient and optical path length through the device. Likewise, the effective radiative current density is given by Equation 1.3,

$$J_{rad} = q(1 - R(E))\epsilon(E)b_a(E) \tag{1.3}$$

with $\epsilon(E)$ being the emissivity, or probability that the surface will emit a photon. Thus in steady state, $\epsilon(E) = \alpha(E)$. If we now expose the cell to a solar flux (or any illumination), b_s, the current density from absorbed photons will change to include contributions from both solar photons and ambient thermal photons,

$$J_{abs} = q(1 - R(E))\alpha(E)\left[b_s(E) + (1 - \frac{F_s}{F_e})b_a(E)\right] \tag{1.4}$$

where F_s and F_e are the solar and cell emission geometric factors, respectively. F_e represents the escape cone for photons ($F_e = \pi\frac{n_0^2}{n_s^2}$) trapped inside a semiconductor with a refractive index n_s and an ambient with a refractive index n_0. Given that we are now absorbing more energy into our material, the relative population of excited electrons is increased; this means that we will have more radiative relaxation events, and hence, a different radiation current. At a semiconductor interface with air ($n_0 = 1$, $F_a = F_e \times n_s^2 = \pi$), the radiative flux under illumination, b_e, is

$$b_e = \frac{2F_a}{h^3c^2}\left[\frac{E^2}{e^{(E-\Delta\mu)/k_BT_a}-1}\right] \tag{1.5}$$

where $\Delta\mu$ is the quasi-Fermi level splitting or the chemical potential of the incident light. This yields a radiative photon flux under illumination of

$$J_{rad} = q(1-R(E))\epsilon(E)b_e(E,\Delta\mu) \tag{1.6}$$

Finally, $\epsilon(E) = \alpha(E)$ still holds, and by taking the difference between Equations 1.4 and 1.6, we can determine net absorption and emission current densities:

$$J_{abs(net)} = q(1-R(E))\alpha(E)\left[b_s(E) - \frac{F_s}{F_e})b_a(E)\right] \tag{1.7}$$

$$J_{rad(net)} = q(1-R(E))\alpha(E)[b_e(E,\Delta\mu) - b_e(E,0)] \tag{1.8}$$

With Equations 1.7 and 1.8, we are set to find expressions for photocurrent and dark current, respectively. To simplify our discussion, we will assume that our semiconductor does not suffer from any reflection losses ($R(E) = 0$), and that it perfectly absorbs every photon with an energy greater than its bandgap, E_g. In this case, the photocurrent, or short circuit current density is determined by integrating Equation 1.7 over all photon energies above the bandgap,

$$J_{SC} = q\int_{E_g}^{\text{inf}} b_s(E)dE \tag{1.9}$$

which demonstrates that J_{SC} is purely a function of bandgap and spectrum. We take a similar approach to derive an expression for dark current, J_0. In an ideal PV element, there would be no non-radiative recombination (i.e. Shockley-Reed-Hall recombination from defects or Auger recombination due to intercarrier collisions), and radiative recombination would be the only pathway for excited electrons to lose energy. If we further assume that our solar cell has a perfect rear reflector, J_0 is simply:

$$J_0 = q\int(1-R(E))\alpha(E)[b_e(E,\Delta\mu) - b_e(E,0)]dE \tag{1.10}$$

In an ideal semiconductor with lossless transport, $\Delta\mu$ is a constant value everywhere and is given by qV_{app}. By adding our photocurrent and dark current together, we come up with an expression which describes the solar cell's IV characteristics under illumination,

$$J(V) = J_{SC} - J_0(e^{qV_{app}/k_bT} - 1) \tag{1.11}$$

Equation 1.11 is shown with respect to power generation being positive. In this case, as V_{app} increases, so does our effective recombination current. This in turn,

reduces the total current out of the device. As voltage continues to increase, the two currents will come to a point where they are balanced; this is the open circuit voltage, V_{OC}. Beyond this applied bias, recombination current will dominate, and the device will behave like a light emitting diode (LED).

The efficiency of a solar cell, η, is measured by taking the ratio of generated power to incident power, P_s as shown in Equation 1.12,

$$\eta = \frac{VJ(V)}{P_S} = \frac{VJ(V)}{\int_0^{\text{inf}} Eb_s(E_s)dE} \tag{1.12}$$

and is maximized when $\frac{d}{dV}VJ(V) = 0$. If we take this ideal device and optimize its bandgap with respect to the solar spectrum, we find a maximum efficiency of about 33% near 1.4 eV. [28] In reality, this idealized device does not exist; reflection losses occur, there is never lossless transport or perfect absorption, and there will always be a finite amount of non-radiative recombination. Despite these challenges, possible paths towards this perfect solar cell and beyond are outlined in the next section.

1.2.3 Methods of Enhancing Solar PV Energy Production

Several methods exist for boosting the efficiency of a solar cell, including tuning material properties and device structures, modifying the incident spectrum and optimizing the load resistance. As discussed in 1.2.2, there is an applied bias where the cell will run most efficiently and this condition can always be satisfied by supplying the appropriate load for solar cell. However, because an individual cell does not supply enough voltage or current, it is more practical to match a load to the maximum power point of a module. [28]

Band gap also plays an important role in PV performance due to its direct relation to the fraction of the spectrum that can be absorbed by a solar cell. If the bandgap is too large, the device won't absorb enough light, and will suffer from a low J_{SC}. While it is possible to upconvert a portion of the solar spectrum, these methods are often costly and inefficient. [29–32] On the flip side, if the bandgap is too small, the device will not generate a sufficient V_{OC} to create adequate amounts of power. Additionally, the excess energy from any photons with $E > E_g$ will be thermalized and lost to heat. There is ongoing research into extracting extra work from hot carrier solar cells, [33,34] yet this problem can be solved in another manner through the use of multijunction solar cells. Dual, triple, or quadruple junction cells offer the possibility of splitting the spectrum into discrete segments to be absorbed by the different materials which comprise the PV stack. This minimizes the problem of hot carriers and efficiencies of 44.7% have been realized using this method. [35] In practice, it helps to know the incident spectrum so that device composition can be tweaked to achieve current continuity throughout the solar cell.

The other downside to multijunction cells are their increased cost, which is a result of their comparatively complex manufacturing requirements.

There the additional problem of direct vs indirect bandgap. Direct bandgap materials such as GaAs and many III-IV compounds have high absorption coefficients, which means that less material can be used when compared to a typical indirect bandgap material. While Si, which has an indirect bandgap, requires ∼10x more material to absorb an equivalent amount of light as GaAs, it remains the most popular PV material because of its relative abundance and low cost. The practical requirements of high optical absorption and perfect charge collection (i.e. no recombination, radiative or nonradiative) mean that device thickness has to be appropriately balanced. Different light trapping and photon recycling schemes are often employed to address this issue by texturing the front and/or rear surfaces of the solar cell. [28]

One of the first assumptions that we made was that our ideal solar cell had no reflection losses, but light passing through any material interface will suffer from Fresnel reflections,

$$R = \left(\frac{n_0 - n_s}{n_0 + n_s}\right)^2 \tag{1.13}$$

If a thin film of a dielectric with refractive index n_1, and thickness d_1 is placed on top of the semiconductor surface, the reflection for an incident beam of wavelength λ and angle of incidence θ_1 becomes,

$$R = \frac{(n_0 - n_s)^2 + (n_0 n_s/n_1 - n_1)^2 \tan^2 \delta_1}{(n_0 + n_s)^2 + (n_0 n_s/n_1 + n_1) \tan^2 \delta_1} \tag{1.14}$$

where $\delta_1 = 2\pi n_1 d_1 \cos\theta_1/\lambda$ is the phase shift of light in the thin film. R is minimized when $\delta_1 = \pi/2$, which occurs when $d_1 = \lambda/4$. Fresnel reflections at an interface can be completely mitigated for normal incidence at a designed wavelength, λ_0 if $n_1 = \sqrt{n_0 n_s}$. Though thin film antireflective (AR) coatings present a simple method of raising efficiency by increasing the amount of light coupled into the PV structure, they can be highly reflective outside of their design parameters because they are designed for a specific wavelength and angle of incidence.

The final method is to concentrate light onto our solar cell; this performs two actions. First, it replaces some fraction of semiconductor with precision mirrors or low-cost plastic optics. This substitution allows for expensive, high efficiency multijunction cells to be used in place of low efficiency silicon cells. Second, it increases the efficiency of the cell by expanding the angular range of the source. By integrating the solid angles as seen by the PV from the concentrator optics and the sun, and taking the ratio, we can define an an enhancement factor, X,

$$X = \frac{\int_0^{2\pi} \int_0^{\theta_X} d\Omega}{\int_0^{2\pi} \int_0^{\theta_{sun}} d\Omega} = \frac{\sin^2 \theta_X}{\sin^2 \theta_{sun}} \tag{1.15}$$

where θ_X is the half-angle range provided by the concentrator optics, and θ_s is the half-angle subtended by the sun (0.26°). The geometric factor F_s is now substituted by $F_X = \pi \sin^2 \theta_X = X \sin^2 \theta_{sun}$, which means that the incident flux, b_s also increases by a factor of X. To first order, $J_{SC}(X, b_s) \approx X J_{SC}(b_s)$. This results in a higher J_{rad} required to offset the enhanced J_{abs}, which for a device with an ideality factor, m, ultimately leads to an increased open circuit voltage:

$$V_{OC} \approx V_{OC,unconcentrated} + \frac{mk_bT}{q} \ln X \tag{1.16}$$

The boost in J_{SC} and V_{OC} make the optimal power generation point higher than would be seen under no concentration [28]. The unfortunate drawback to concentrator photovoltaics (CPV) is that it complicates what could be an otherwise simple system. In order to achieve high concentration, active single-, or even dual-polar axis tracking is oftentimes required to maintain focal alignment and depending on the level of concentration used, active cooling may also be required. Nevertheless, when appropriately managed, CPV can be used to make incredibly efficient modules at price points similar to traditional flat plate, Si-based PV.

1.3 A Brief Review of State-of-the-Art CPV Technologies

There are various levels of concentration for a CPV system categorized as low-X (1-10x, LCPV), medium-X (10-100x, MCPV), and high-X (100-1000x, HCPV). As the main point of a CPV system is to provide strong cost leverage for expensive high efficiency PVs through the substitution of cheap plastic optics [36] we will focus our attention on HCPV systems. Due to the relatively small amount of semiconductor required, HCPV (hereby noted simply as CPV) systems are most often coupled to near-record efficiency multijunction cells, and can have module efficiencies greater than 35%. [37, 38] Before we continue on to the bulk of this thesis, we will briefly review several types of modern CPV designs that are available commercially, as well as those being presently researched.

1.3.1 Fresnel-based CPV Designs

In its most basic form, CPV is a non-imaging optics problem; it isn't important to form an image at the front surface of the solar cell, rather, we want to maximize the amount of energy coupled to our PV, ideally with a nominally uniform flux distribution at that surface. [39] Perhaps the most common type of CPV system utilizes a large Fresnel lens in conjunction with a single- or dual-axis polar tracking system to maintain focal alignment as seen in Figure 1.2. In this instance, the Fresnel lens is essentially forming an image of the sun on the solar cell, and

Figure 1.2. Soitec's FLATCON module which utilizes only a single Fresnel lens to couple light to multijunction PVs. This particular design set a world record for module efficiency at 36.7% in July of 2014.

due to its discontinuous shape, that image is blurred at its edges, leading to a bell-shaped irradiance distribution. [40] Moreover, chromatic aberration resulting from dispersion effects as light of varied wavelengths travels through the lens leads to different focal spots for each spectral band, which can be undesirable for multijunction cells. Implementing dome-shaped Fresnel lenses can decrease both focal and chromatic aberration at the cost of increased manufacturing complexity. [41]

Fresnel lenses for CPV are usually fabricated via one of two approaches/material combinations: injection molding polymethymethacrylate (PMMA, or acrylic) to the desired form, or by attaching silicone Fresnel facets to a glass cover, termed silocone-on-glass (SoG). Each system has its own merits and downfalls. Acrylic Fresnel lenses are lightweight, simple to mass produce, and because they are made from a single material, have a low shift in chromatic aberration and focal length as a function of temperature. As a polymer, PMMA is soft and prone to abrasive weathering or other types of environmental degradation. Additionally, it is also sensitive to oxidative photodegradation; while certain additives mitigate these effects and help to prolong the life of the lens, these weaknesses run contrary to a low maintenence, low cost system. SoG Fresnel lenses have higher chemical stability, higher transmittance over a wider spectral range, and the glass substrate acts to protect the Fresnel facets from the environment. However, SoG lenses are heavier than their acrylic counterparts, are more susceptible to temperature-induced chromatic aberration at large temperature differentials, and depending on the grade or type of glass used, UV-induced solarization can reduce the transparency of the substrate. [42] All of these factors should be considered when selecting materials

for a Fresnel-based CPV system.

As previously mentioned, it is possible to obtain high levels of optical gain with a single-optic system, the inhomogeneity in the irradiance pattern can lead to series resistance losses and cell heating, both of which contribute to diminished system performance and lifetime. [43] The addition of a secondary optical element (SOE) near the surface of the solar cell, such as a hollow inverted truncated pyramid reflector, a refractive truncated pyramid (Figure 1.3a-b, respectively), ball lens, [44] or a free-form surface [45] can enhance to the total acceptance angle of the system, act to minimize reflection losses between the air-PV interface, and greatly increase the focal spot uniformity. One final method to ensure focal uniformity for a Fresnel based concentrator is to create a Köhler integrator, a technique common for homogenizing illumination systems. However, instead of using multiple sets of optics to concentrate, homogenize, and collimate light, it is possible to collapse all of these functions into the faceted Fresnel and a free-form SOE [45, 46] surfaces as can be seen in 1.3c. Employing such systems allow for single-cell concentrators with efficiencies close to present records, [41] with the added benefits of an increased acceptance angle that relaxes tracking constraints, and potentially longer cell lifetime resulting from the more uniform distribution of light (and heat) on the PV.

1.3.2 Reflective CPV Designs

Many of the same ideas from Fresnel-based CPV apply, except that instead of a Fresnel lens as the primary optical element, it is typically either a parabolic or free-form mirror. One of the major advantages of mirror-based systems is that they do not suffer from chromatic aberration, as light is reflected from the mirror surface rather than refracted through a dielectric; second-surface silvered parabolic mirrors have optical efficiencies from ∼94% up to a solar-weighted optical efficiency of 95.4% [47] with the addition of antireflective coatings, whereas their Fresnel lens counterparts are closer to ∼85%, owing to wavelength dependent Fresnel reflection losses and transmission coefficients. At the same time, mirrors are not without their faults, as they tend to be expensive. Parabolic mirrors are generally made large to offset costs and as a result of their size, have very high optical gains. Beyond 500x, non-uniformity of the focal spot as a consequence of coma aberration is exacerbated, and the mirror needs to be supplemented by secondary or tertiary optics to make the best use of the concentrated light. [48]

SOEs similar to those found in Fresnel systems can be used to homogenize the flux distribution at the PV surface. Cassegrain concentrators are a particularly common solution, [48] requiring a secondary mirror at an intermediate plane that serves to fold the optical system and direct light back towards the PV, as seen in Figure 1.4a. The addition of a piece of cover glass serves to protect the delicate mirror surface from the environment, thereby increasing the longevity of the system. A major drawback to Cassegrain-type designs is that they can generally only focus

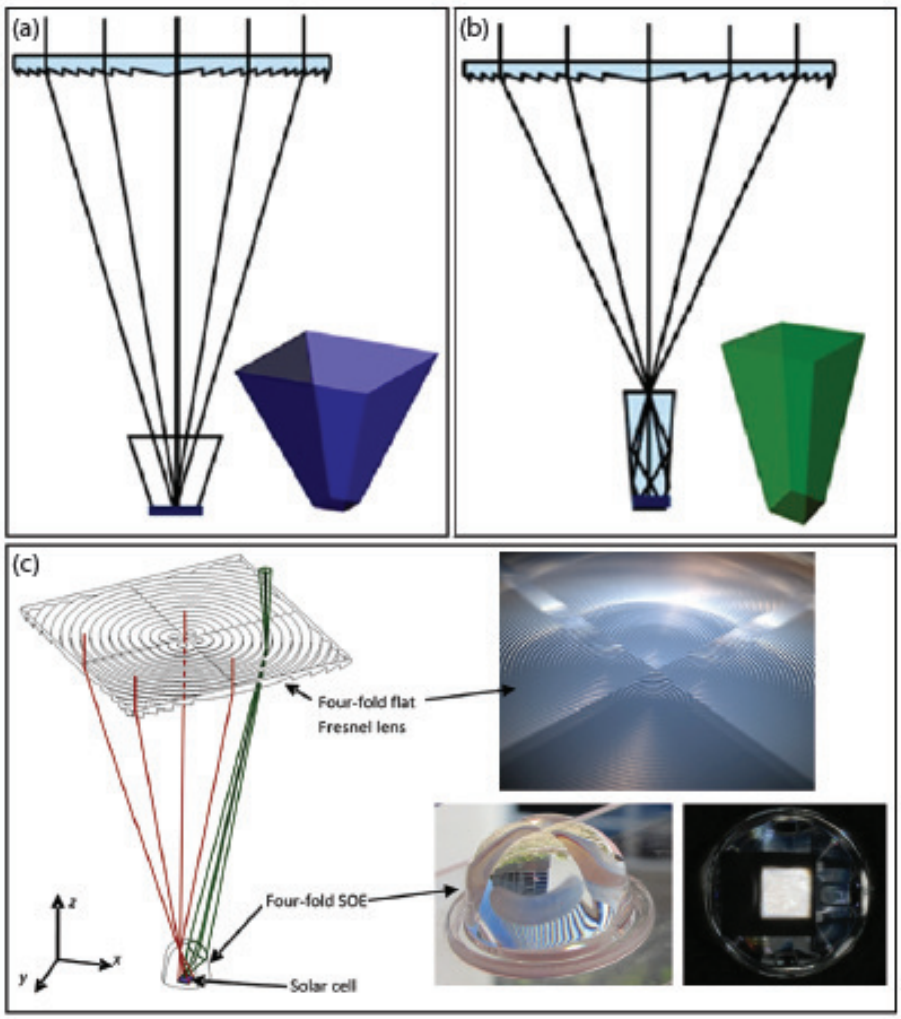

Figure 1.3. Examples of different SOEs. (a) A hollow inverted truncated pyramid reflector increases homogeneity and the acceptance angle by reflecting light towards the PV (b) A refractive truncated pyramid uses total internal reflection to homogenize incoming light. (c) A fourfold Fresnel-Köhler concentrator with a free-form SOE, along with pictures of the prototypes, and a demonstration of the uniform irradiance pattern at the cell. Images compiled from ref [41]

to a single cell, which tends to necessitate some form of active heat removal; given that parasitic losses from cooling systems can consume nearly 10% of the power generated from such a CPV module, it is desirable to distribute the incident energy more evenly. A recent design from the University of Arizona uses a large parabolic dish, not unlike one that you might find used for a telescope, coupled to a secondary ball lens and 36 tertiary XTPs to disseminate light evenly among the same number of multijunction cells at a gain of 1200x. By spreading power evenly among the cells, the total cooling losses dropped to a mere 2% of the total electrical output

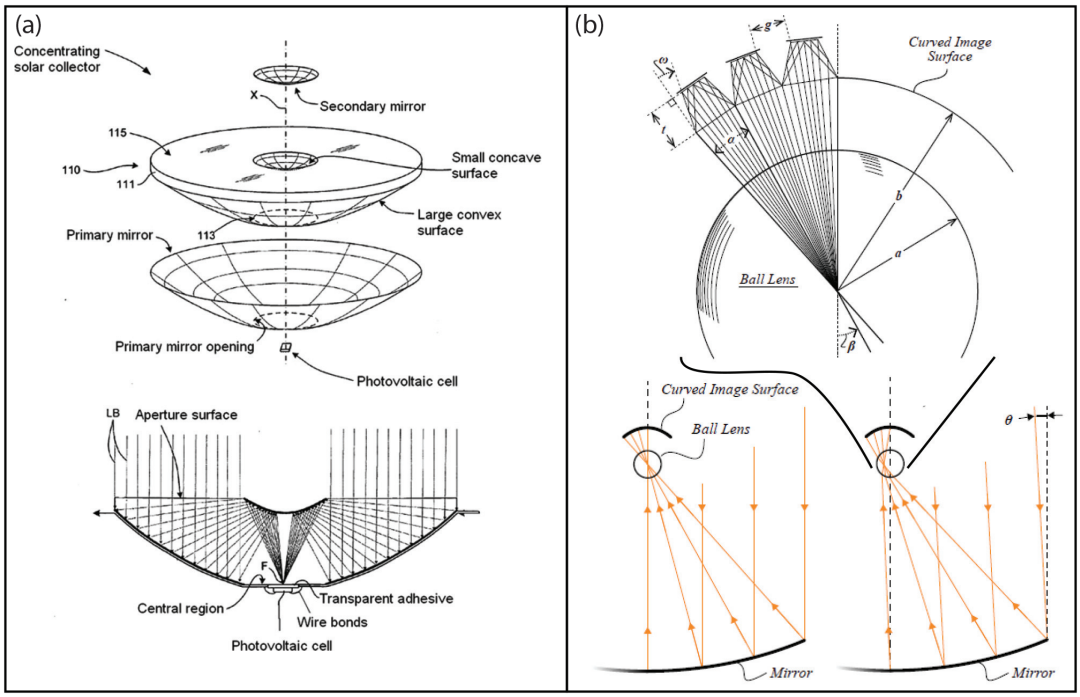

Figure 1.4. Different types of mirror-based concentrator designs. (a) A Cassegrain concentrator with glass cover to protect the mirror surfaces. [48] (b) Novel dish-based CPV by ref [49] that utilizes Köhler optics to homogenize the incident flux and direct it to a number of PVs. Provided that light is incident within the acceptance angle of the system, XTPs aim to increase the uniformity of the concentrated light onto the solar cell.

of the system. [49] Furthermore, this design allows for the easy exchange of next generation multijunction cells with even higher efficiency.

Both the Köhler and Cassegrain design concepts were already mature before they were transitioned into the realm of CPV. A much more recent development in CPV and the optics community is the addition of the simultaneous multiple surfaces (SMS) 3D method to optimize free-form surfaces. [50] While the vast majority of high concentration designs have acceptance angles between ±0.2-1°, these arbitrary surfaces can obtain acceptance angles as large as ±1.85° at 1000x concentration levels. [41].

Many of the reflective CPV systems discussed thus far effectively shade a portion of their collection area due to their use of secondary optics. Fresnel-based designs minimize this effect, but they suffer from lower optical efficiencies. If one substitutes the faceted rings of a Fresnel lens with mirrors (spherical or parabolic), they can in effect obtain the high optical efficiency of a parabolic mirror system with the rear-focusing capabilities of a lens. [51] Moreover, each mirror ring creates a quasi-gaussian distribution at the focal plane, so granted that the mirrors are close enough to one-another, no homogenizing optics are needed.

1.3.3 Planar CPV Designs

To this point in our brief CPV review, all of the designs have been constrained to dual-polar axis tracking systems due to the nature of their small acceptance angles. While simple and effective, this mode of tracking demands robust and often costly mechanical tracking infrastructure to adequately control the movement of large-area CPV modules, especially in windy conditions. [52] Moreover, orientation-based CPV systems have limited siting capability that prevents them from integration in urban environments or on rooftops due to their unwieldy nature and the need for large land area to avoid shading among adjacent systems. [53, 54] If some of the solar tracking functionality were to be integrated into the CPV module, at the very least, there is potential to reduce the tracking system a single polar axis, thereby enhancing system robustness and decreasing costs.

Various translation-based CPV tracking strategies have been proposed as an alternative to polar tracking designs, in which the position of the PV cells and/or multiple concentrator optics are varied laterally with respect to one another. This notion has been explored in the context of mobile freeform optics [55, 56] and planar waveguide concentrators, [57, 58] however a general difficulty among these approaches is significant deterioration of the concentration ratio at wide (>20° from normal) incidence angles. Because only 17% of annual solar illumination incident on a fixed, latitude-tilted panel over the course of a typical 8-hour day occurs at incidences <20°, the utility of planar tracking has been limited to date.

One avenue of increasing the acceptance angle and reduce scattering losses for a refractive system is to use a traditional convex lens in place of a Fresnel lens as the primary optic. While this would dramatically increase material costs for large-area concentrators, if both the optics and PV elements are scaled to maintain gain, it becomes justifiable to transition to continuous lenses. Although reducing the size of the optics and PV elements places an increased stringency on manufacturing tolerances, it also spreads heat more evenly throughout the system, meaning that external heat sinks are no longer required. [53] Additionally, it has been shown that as the size of high efficiency concentrator cells decrease, series resistance losses from focal spot inhomogeneity are minimized, even for concentration factors exceeding 1000x. [59, 60] Owing to recent advances in semiconductor processing technologies, it is now feasible and cost effective to grow large quantities of GaAs or multijunction micro-PVs (<1 mm on a side) as releasable stacks in an affordable manner, making the transition to smaller systems all the more attractive. [61, 62] However, in order to have a microcell-enabled planar solar concentrator, we must first solve problems relating to the small acceptance angles of a typical planar system.

1.3.3.1 Optimizing a Planar Design for Full-Day Operation

Figure 1.5a illustrates the notion of fully planar CPV tracking, where a solar cell is translated laterally to follow the focal point of a fixed lens as it moves in response

to different solar incidence angles over the course of a day. A major challenge for this approach stems from Petzval curvature of the image plane indicated by the dashed line, where on- and off-axis light concentrates in different axial planes. This effect significantly reduces the optical efficiency of the concentrator for sunlight incident at angles >20° since the focal point no longer coincides with the plane of the solar cell. [57]

Petzval curvature can be minimized by appropriately combining optical elements with positive and negative surface powers as in the case of a common fish-eye lens. In general however, wide field-of-view lens systems require multiple elements, leading to high reflection loss, excessive size, weight, and cost that are all in opposition all to the goal of an efficient, inexpensive planar concentrator. Alternatively, the Petzval surface can be flattened within a single dielectric by combining refraction from a convex front surface with reflection from a concave rear surface as shown in Figure 1.5b to fold the optical path and achieve an intermediate focal plane between the two. To first order, this is understood from the Petzval sum [63] for this configuration,

$$\Sigma = \frac{1-n}{nR_r} + \frac{2}{nR_m} \tag{1.17}$$

which is nulled when the refractive index, n, together with the refractive (R_r) and reflective (R_m) surface radii of curvature satisfy:

$$\frac{R_m}{R_r} = \frac{2}{n-1} \tag{1.18}$$

In contrast to the singlet lens in Figure 1.5a, it is immediately evident from ray tracing that the Petzval curvature in the folded path optic of Figure 1.5b has been virtually eliminated. The result is a dramatic improvement in the concentrator acceptance angle summarized in Figure 1.5c, where a geometric gain of 450, defined as the lens aperture area relative to the spot size enclosing 95% of the power in the focal plane, can be maintained up to ±60° incidence. As shown in Figure 1.5d, this acceptance angle range enables the concentrator to operate year-round, 8 hours per day in State College, PA when fixed at latitude tilt (408°) according to solar incidence predicted by the National Renewable Energy Laboratory Solar Position Algorithm. [64] This is equivalent to being able to concentrate 88% of annual energy incident on a static-tilt panel.

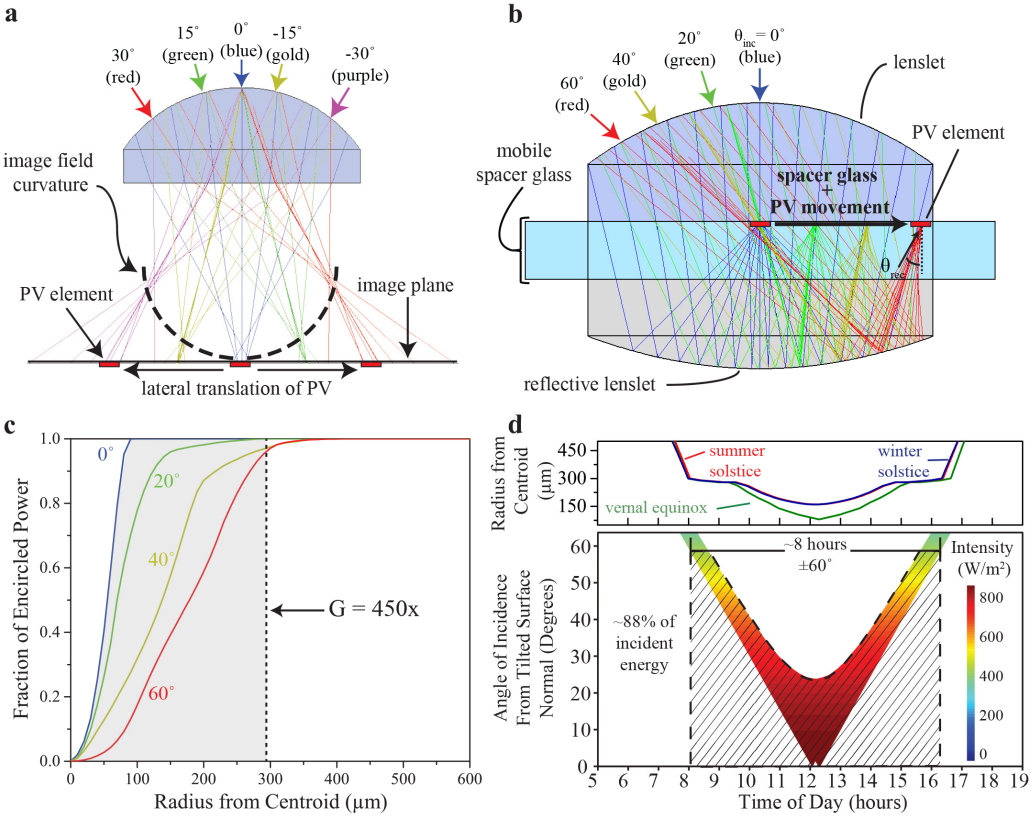

Figure 1.5. (a) Ray-tracing schematic of a singlet lens used for translation-based solar tracking, where defocusing at wide incidence angle due to Petzval curvature leads to poor performance. (b) Elimination of Petzval curvature through use of a folded optical path, where the focal plane lies in the middle of a dielectric with refractive upper and reflective lower surfaces. In practice, the solar cell (red rectangle) is fixed to a central glass or acrylic sheet that slides between upper and lower lenslets lubricated by index-matching oil. (c) Fraction of encircled optical power in the focal plane as a function of radius from the intensity maximum for the configuration shown in (b). The top and bottom lenses consist of acrylic plastic and have a diameter of 12.7 mm; the simulation is conducted for wavelengths λ<1.1 μm using the AM1.5D intensity spectrum. (d) Annual range of solar incidence angles (relative to the surface normal) for a latitude-tilted panel over the course of a year in State College, PA. The false color overlay indicates the approximate direct solar irradiance falling on the panel surface accounting for cosine projection loss. The upper plot displays the calculated focal spot size for the configuration in (c), defined as the spot radius encircling 95% of the focal plane optical power, versus time of day for the annual solstices and equinoxes.

Chapter 2
Simulation, Design, and Validation of the Planar Microtracking Paradigm

This chapter provides further simulations for the planar microtracking solar concentrator as well as experimental results. A single cell design is first verified using off-the-shelf optics from Thorlabs. Through the utilization of printed optics, a low-cost concentrator array prototype was fabricated; both designs were tested indoors using a solar concentrator and outdoors on a sunny day. Finally, comparisons to an archetypal dual-polar axis tracking design and a flat-plate silicon panel are made.

2.1 Single Element PV Concentrator Built From Off-the-Shelf Optics

The concept of a folded optical stack can be practically extended in the form of a lenslet/mirror array to form a complete CPV panel as seen in Figure 2.1a illustrates how a folded optical stack can be practically extended in the form of a lenslet array to create a complete CPV panel. Here, matched upper refractive and lower reflective lenslet arrays made of acrylic plastic sandwich a central (glass or acrylic) sheet with a corresponding transfer-printed array of high efficiency microcell photovoltaics (side length < 1 mm). The central sheet slides freely between the lenslet arrays lubricated by index matching oil that also functions to eliminate parasitic reflection losses. Hexagonal tiling is chosen because it leads to higher azimuthal symmetry than, e.g. a square lenslet array and therefore helps reduce corner-related optical losses.

Figure 2.1b summarizes the simulated performance of this concentrator, optimized for 0.7 x 0.7 mm^2 square microcells at a geometric gain, G= 255,

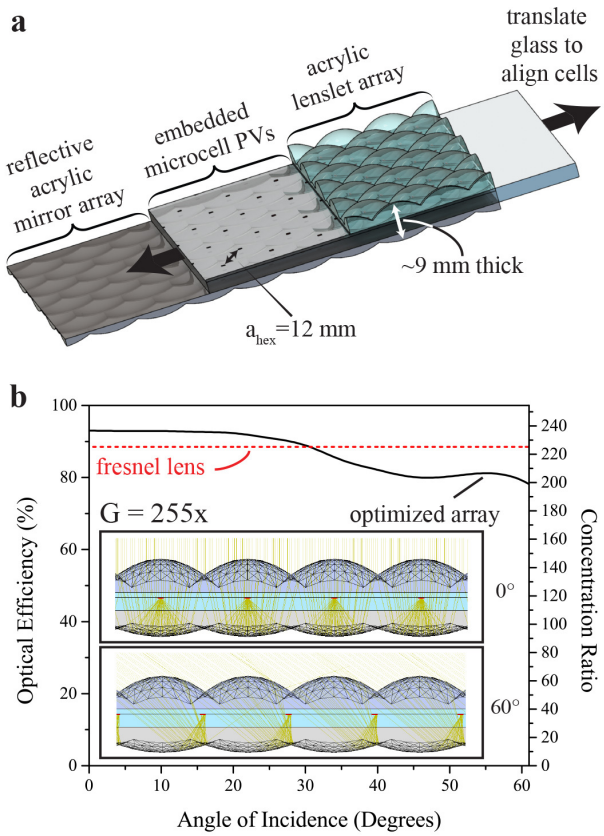

Figure 2.1. (a) Schematic illustration of a microtracking microcell CPV panel. An array of microcell photovoltaics is transfer-printed on a central acrylic sheet that tracks by sliding laterally between stationary upper and lower acrylic lenslet arrays lubricated by index matching oil. (b) Simulated absolute optical efficiency of the array in (a), defined as the fraction of incident optical power in AM1.5D solar spectrum (λ<1.1 μm) delivered to the surface of the microcells. The microcell dimensions are 0.7 x 0.7 mm^2 whereas the lattice constant of the lenslet array is a_{hex}=12 mm, yielding a nominal geometric gain G=255. The maximum lateral translation required at 60 ° is 4.9 mm and the total thickness of the panel is 9 mm. For reference, the simulated optical efficiency of a standard Fresnel lens operating at normal incidence with the same geometric gain is indicated by the red dashed line. The inset shows a cross-sectional ray tracing view of the array at normal (0°) and oblique (60°) incidence angles.

$$G = \frac{\sqrt{3}a_{hex}^2}{2a_{cell}^2} \tag{2.1}$$

where a_{hex} and a_{cell} are the hexagonal lattice constant and microcell side length, respectively (i.e. G is the ratio of lenslet to microcell area). At normal incidence, the fraction of optical power delivered from the concentrator surface to the microcell array is $\eta_{opt} = 0.93$, essentially that of a second surface mirror, with losses due only

the air/acrylic (no anti-reflection coating is assumed) and acrylic/Ag reflectance. Consistent with Figure 1.5b, high optical efficiency $\eta_{opt} > 0.79$ is maintained up to $\theta_{inc} = 60°$ incidence. Defining the flux concentration ratio,

$$CR = G\eta_{opt} \tag{2.2}$$

as the increase in average intensity received by the microcells relative to that at the concentrator surface therefore results in CR>200 maintained over the entire range of incidence angles, with negligible dependence on azimuth. This result compares favorably with the reference case of a standard acrylic Fresnel lens operating at normal incidence with the same G=255 geometric gain indicated by the red dashed line (η_{opt}=0.89, CR=225). Optical losses due to shading by the bus line electrical interconnects to each cell are not included in Figure 2.1. Shading loss is estimated in the range 1-11% depending on the bus line width, the thickness of the concentrator stack, and the angle of incidence.

To explore these predictions, a 0.7 x 0.7 mm^2 GaAs microscale photovoltaic cell (thickness ~3 μm) was fabricated and transfer printed onto 1 mm thick B270 glass selected for insertion between two off-the-shelf, 12.7 mm diameter plano-convex BK7 lenses with focal lengths f=15 mm and f=30 mm for the upper and lower elements, respectively. A 150 nm thick layer of Ag was evaporated onto the lower lens surface and the trio was index matched together with oil as shown in Figure 2.2a for testing under collimated, broadband illumination from a Xe lamp (see Figure B.1 in Appendix B for details). The current-voltage characteristic of a typical microcell under one sun illumination is displayed in Figure 2.2b; performance metrics are detailed in Supplementary Figure B.3.

Figure 2.2c presents the short-circuit current density measured for the bare microcell (J_0) together with that integrated in the concentrator stack (J_{CR}) as a function of incidence angle. Since the photocurrent is directly proportional to absorbed optical power, the difference marks a roughly constant 210-fold increase in the average intensity delivered to the microcell (i.e. $CR \approx$210) for incidence angles ranging up to $\theta_{inc} = 55°$ that is reproduced in simulation as shown in Figure 2.2d. As indicated by the red dashed line, this increase is nearly equivalent to that obtained at normal incidence using the bare microcell and a plastic Fresnel lens with the same geometric gain (G=260). Because the photocurrent angle dependence in each case follows the cosine projection intensity loss designated by the red lines in Figure 2.2c, the optical efficiency of the concentrator itself is largely independent of incidence angle. It is estimated on the right-hand axis of Figure 2.2c according to

$$\eta_{opt} \approx \frac{J_{CR}T_{ac}}{GJ_0 < T_{cc} >} \tag{2.3}$$

where $T_{ac}(\theta_{inc})$ is the spectrally-averaged Fresnel transmittance from air into the microcell and $< T_{cc} >$ is that from glass into the microcell averaged over the range of angles, θ_{rec}, indicated in Figure 1.5b.

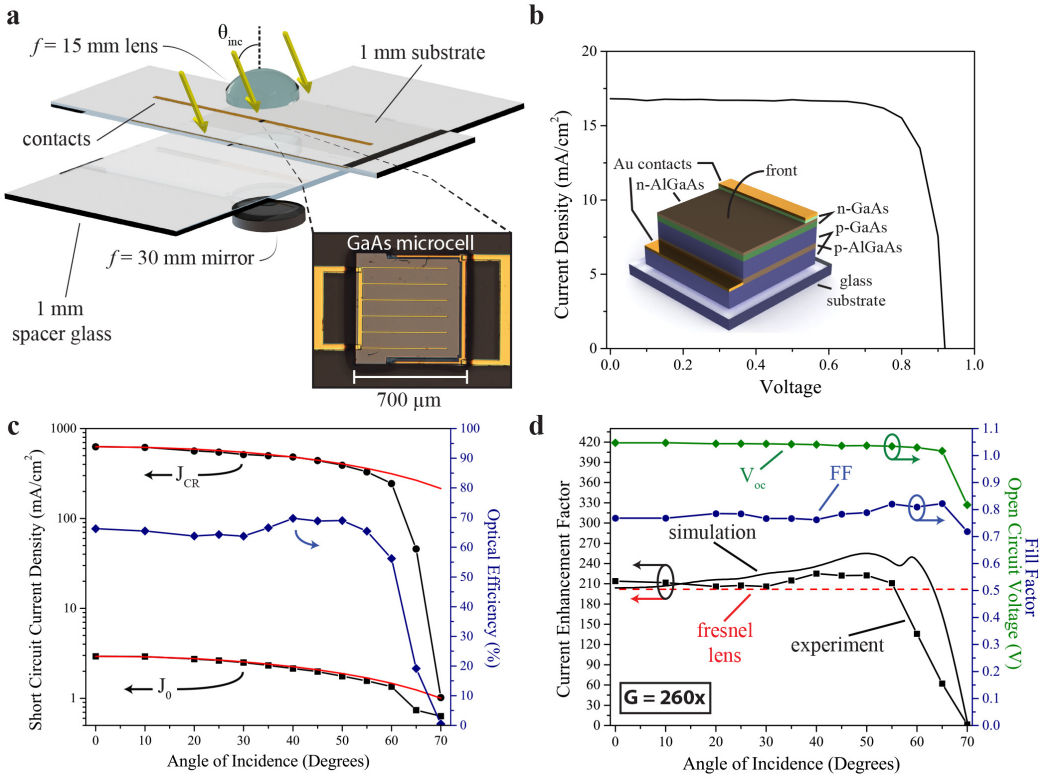

Figure 2.2. (a) Schematic of the testing arrangement for a single 0.7 x 0.7 mm^2 GaAs microcell using 12.7 mm diameter plano-convex BK7 glass lenses. (b) Current-voltage characteristics measured for a typical microcell under AM1.5D simulated solar illumination. The inset shows a diagram of the device architecture. (c) Short-circuit current density measured under collimated Xe lamp illumination as a function of incidence angle for the microcell located in (J_{CR}) and out (J_θ) of the concentrator (i.e. the bare cell), respectively. The red lines indicate the cosine projection loss relative to normal incidence. Optical efficiency on the right-hand axis represents the fraction of incident power delivered to the microcells and is calculated as described in the text. (d) Simulated and measured current enhancement factors together with the microcell fill factor and open circuit voltage (in the concentrator) as a function of incidence angle. The red dashed line indicates the current enhancement obtained for the same microcell at normal incidence using an acrylic Fresnel lens with the same 12.7 mm diameter aperture size.

A potential concern with this method of concentration is non-uniform illumination of the solar cell, which can decrease both open-circuit voltage (V_{oc}) and fill-factor (FF) owing to lateral current flow that increases series resistive loss. [43] It is notable then in Figure 2.2d that V_{oc} and FF are largely independent of incidence angle for the concentrated microcell, suggesting that the changing illumination profile is not a significant concern. This is presently ascribed to the small microcell dimensions, which reduce the path length and thus voltage drop from lateral current

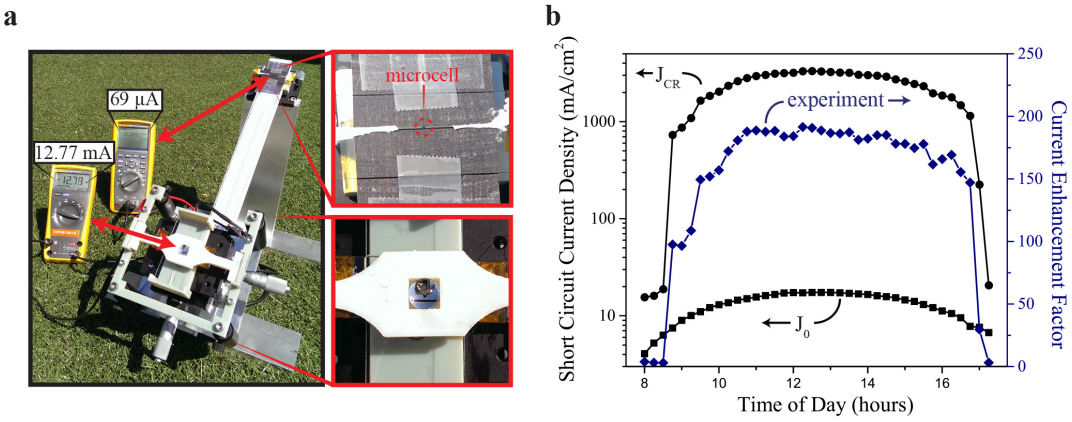

Figure 2.3. (a) Photograph showing the concentrator outdoor testing configuration; the insets provide more detailed views of the concentrator and bare cell reference. (b) Short-circuit current density recorded from the bare and concentrated microcells at 15 minute intervals throughout the day on May 31, 2014 in State College, PA, USA; the right-hand axis displays the current enhancement factor.

flow. Similarly, microcell dimensions are expected to mitigate thermal loading since the lower absolute power dissipated at each cell location distributes heat over the entire module more effectively; [59, 60] no active cooling was used in any of our measurements.

The concentrator stack was subsequently tested outdoors on a sunny day (May 31, 2014) tilted at latitude in State College, PA, USA from 8 am to 6 pm by manually adjusting the translational alignment every 30 minutes. Figure 2.3a presents a photograph of the testing arrangement showing the short-circuit current measured for neighboring microcells located in and out of the concentrator stack. As shown in Figure 2.3a, the concentrator operates effectively throughout the day, maintaining a short-circuit current enhancement in the range 150 - 200x from 9 am to 5 pm. This result is in reasonable qualitative agreement with the enhancement determined under laboratory testing (Figure 2.2d) and thus, together with open-circuit voltage and fill-factor that were similarly maintained, equates directly to the increase in power output (see Figure B.2 in Appendix B for details).

Figure 2.4 explores the illumination profile and microcell positioning tolerance in more detail by mapping the photocurrent as a function of cell position relative to the focal point c.f. Fig. 2.4a. These measurements demonstrate an alignment tolerance of approximately ± 0.1 mm at normal incidence in Fig. 2.4b that decreases to ± 0.05 mm at $\theta_{inc} = 60°$ in Figure 2.4d, consistent with the respective simulations in Figure 2.4c and 2.4e. The asymmetric nature of the photocurrent map at wide angle results from elongation of the focal spot and is due in part to the use of off-the-shelf spherical lenses; generally, the wide angle performance can be improved by optimizing toward hyperbolic surface curvature and/or adding aspheric terms.

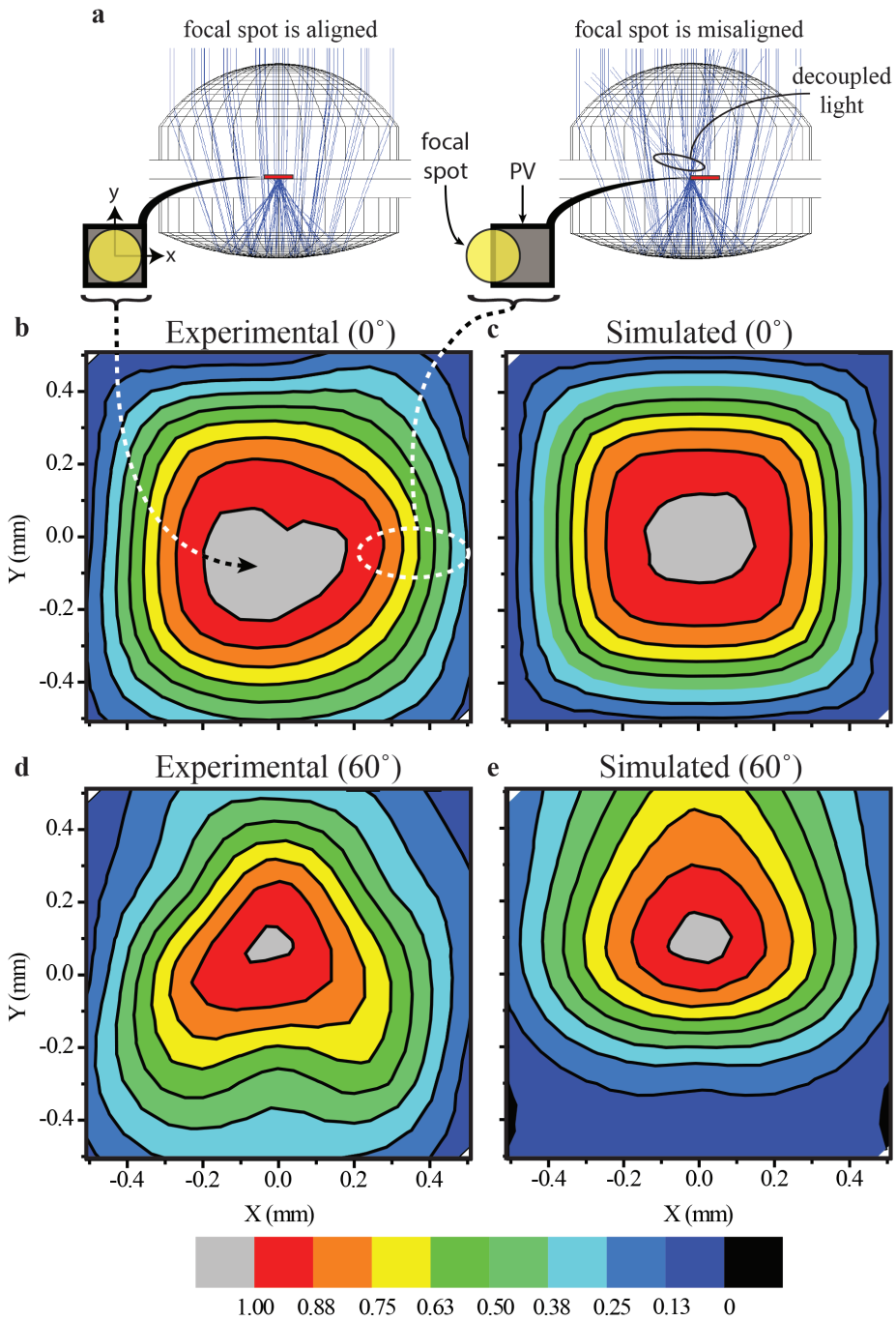

Figure 2.4. (a) Schematic illustration of microcell positioning tolerance measurement, where short-circuit current is recorded from the microcell as it is translated laterally in a grid of locations centered about the focal spot centroid. The resulting contour plots in (b) - (e) constitute a convolution between the microcell active area and the focal spot intensity distribution; in each plot the data are normalized to the maximum (aligned) value for ease of comparison. Qualitative agreement is observed between the measurement (b) and ray tracing simulation (c) at normal incidence with a misalignment tolerance of approximately ±0.1 mm. As the focal spot elongates and increases in size, the tolerance narrows to roughly ±0.05 mm for 60° incidence in both measured and simulated data of (d) and (e), respectively. Contours for the experimental data in (b) and (d) are generated from interpolation of an original 5 x 5 grid of data points.

2.2 Concentrator Array Utilizing 3D-Printed Optics

Due to the cost and time associated with fabricating custom lenslet arrays via conventional diamond-turning or precision molding techniques, we exploited recent development in 3D-printed optics to fabricate and test a complete, small-scale microcell CPV array. While 3D printing has begun to revolutionize rapid prototyping in many other fields, [65–67] the goal of printing high-quality optics has remained elusive due to the stringent tolerances imposed on surface error and roughness. The "printoptical" technology [67] employed here aims to address this challenge through controlled buildup and flow of inkjet-printed acrylic plastic, which enables smooth optical surfaces without the need for tooling or post processing.

Figure 2.5a shows the result for a small-scale, 7-element hexagonal lenslet array on acrylic plastic together with a corresponding array of GaAs microcells transfer-printed on a glass substrate. These components were assembled as shown schematically in Figure 2.5a to yield a full concentrator stack approximately 1 cm thick with each series-connected row of microcells contacted independently (details provided in Figure B.4 in Appendix B). Figure 2.5b displays the ratio of net short-circuit current measured in and out of the concentrator stack along with that predicted by ray tracing simulation. Here, we observe a peak current enhancement ratio of ∼150 that is substantially lower than predicted for the design target. This difference is similar to that measured for a single cell from the array, indicating that surface error in the printed lenslets (as opposed to misalignment of the microcell array positions) is the main factor leading to subpar performance. Although precision interferometry [68] was not available to rigorously characterize the lenslet surfaces, profilometry of a small section of printed lenslet along with the aberration induced in a Gaussian beam and a comparison of simulated concentrator performance (red line) all suggest that relatively large scale defects and surface curvature error (∼20%) are responsible for the lower-than-expected performance (see Figure B.5 for details).

Despite the lenslet fabrication error, which could be improved by refining the printoptical process or using molded optics, the initial result in Figure 2.5b demonstrates that the requisite microcell patterning and alignment can be achieved, validating the notion of a larger scale microtracking microcell CPV array. To this point, Figure 2.5c presents outdoor testing results for the prototype array conducted in State College, PA, USA on June 1, 2014, where the concentrator maintains a current enhancement ratio in the range 100 - 150x relative to the bare reference cell for over six hours.

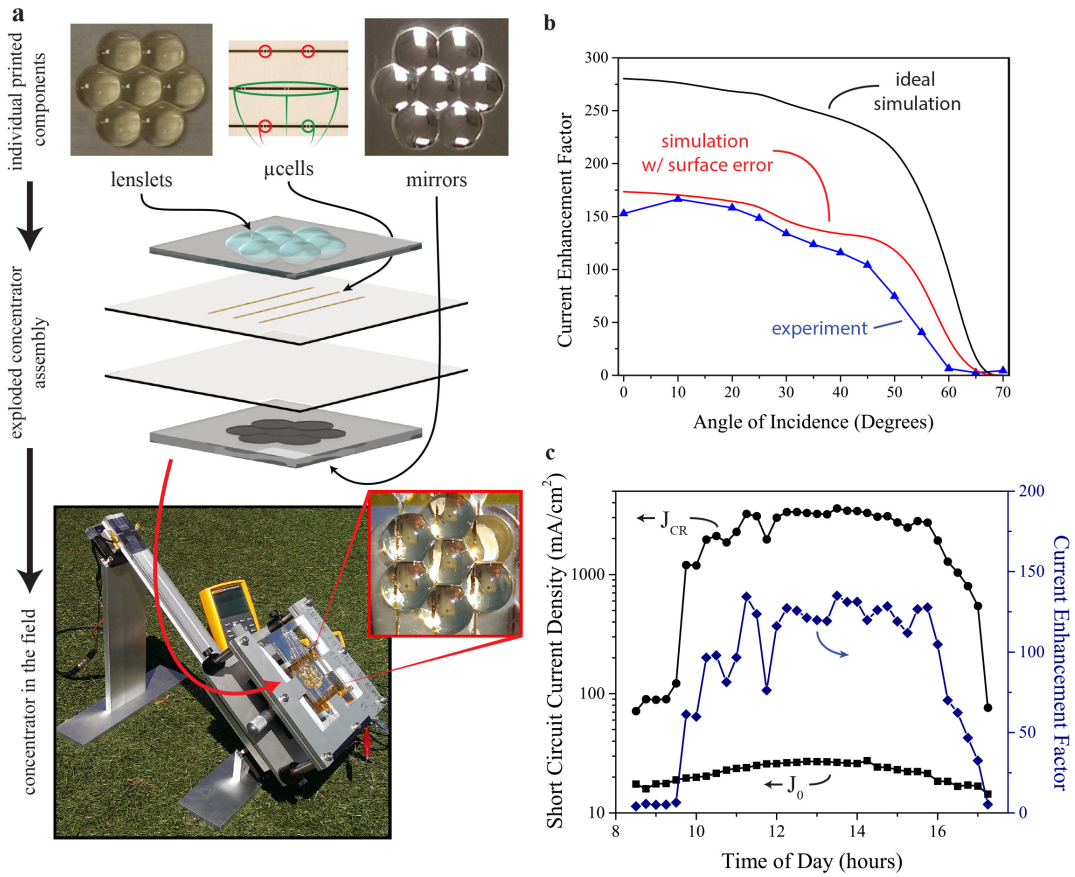

Figure 2.5. (a) Photographs showing the refractive top and reflective bottom 3D-printed lenslet arrays together with the corresponding layout of GaAs microcells used to construct the concentrator prototype. These components were assembled as illustrated in the diagram to create the full concentrator stack shown in photographs of the outdoor testing configuration at bottom. The cells circled in red (top) were damaged during assembly and excluded (by shorting across them) from measurements; the total photocurrent is the sum of that collected from the bottom right cell and the series-connected middle row of three cells circled in green. (b) Ratio of the short-circuit current recorded from the concentrator stack under collimated Xe lamp illumination relative to that recorded for the bare microcell array outside the concentrator. The measured photocurrent gain is substantially lower than that predicted for this design via ray tracing simulation (solid black line) due to surface error in the printed lenslets. Qualitative agreement with the simulation is obtained by incorporating Gaussian surface scatter into the ray tracing model to simulate large-scale surface roughness (red line). (c) Short-circuit current recorded from the prototype array and from the bare reference under full day outdoor testing as shown in (a); the current enhancement ratio is indicated on the right-hand axis.

2.3 Comparison to the Archetypal Dual-Polar Axis Tracking Concentrator utilizing Fresnel Lenses

Cosine projection loss constitutes a fundamental concern for fixed-tilt solar concentration.
Whereas polar tracking maintains sunlight at normal incidence, the intensity falling on a fixed panel decreases as the cosine of the incidence angle and thus, per unit panel area, a fixed-tilt system is inherently less efficient than a polar tracking system. This difference is quantified in Figure 2.6b, which compares the hourly power output per unit panel area at the vernal equinox in State College, PA, USA for an optimized microtracking panel with a conventional Fresnel lens at equivalent 255x geometric gain assuming a solar cell efficiency of 30%. [44, 69, 70] Integrated over the day, the polar tracking CPV system delivers approximately 1.5x more energy than the fixed-tilt microtracking system, typical of the difference throughout an entire year.

By the same measure however, polar tracking panels must be spaced farther apart to avoid shading one another as illustrated in Figure 2.6a and thus cosine projection loss is offset when power generation per unit installed land area is the relevant metric. Because microtracking panels can be spaced closely in the east-west direction without shading one another, more power generating capability can be located in a given area of real estate than for polar tracking systems. As shown in Figure 2.6c, microtracking PV consequently delivers more power per unit land area over the majority of a typical day, resulting in an approximate 1.9x increase in energy output. Compared with an equivalent installation of conventional Si photovoltaics (assuming a module efficiency of 18%; gray line), we project a 30% increase in daily energy output delivered by the microcell CPV system.

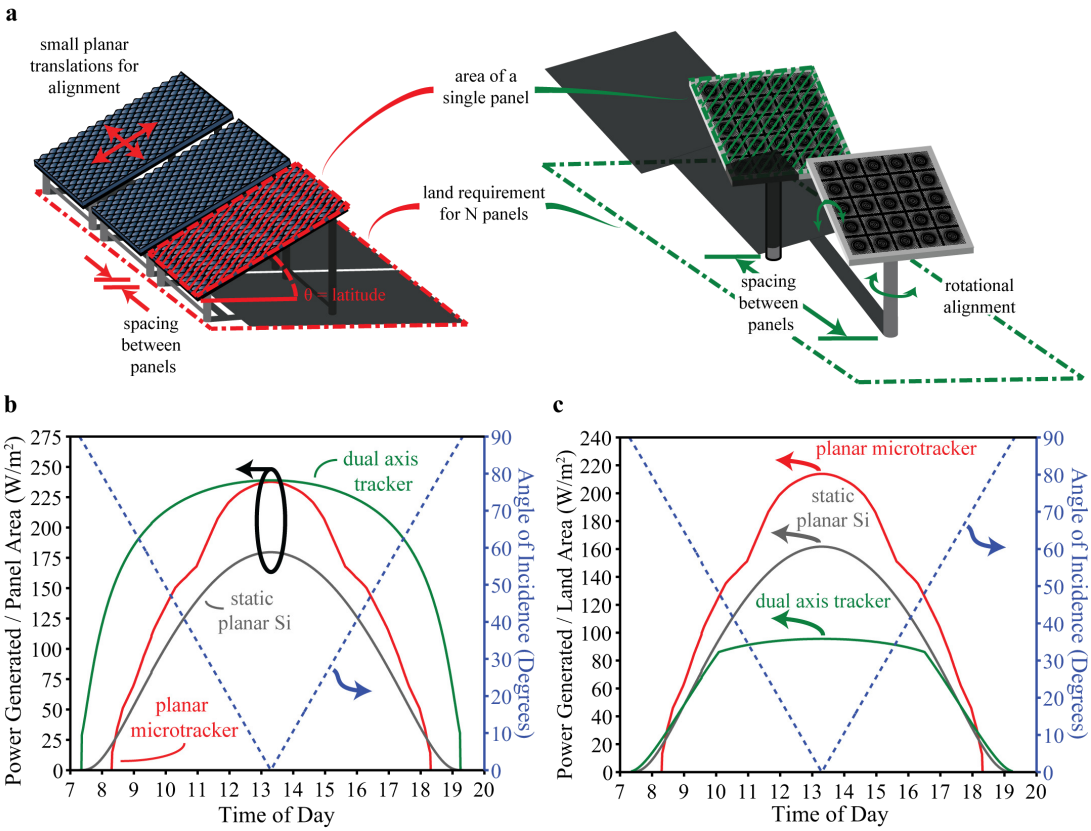

Figure 2.6. (a) Physical layout of an east-west oriented line of latitude-tilted microtracking panels spaced adjacent to one another. Dual axis tracking conventional Fresnel-based CPV panels shown for comparison must be spaced farther apart to avoid shading one another. (b) Simulated power generation per unit panel area for the microtracking and dual axis systems in (a); spacing between the dual axis panels is unconstrained and large enough to entirely avoid shading. The dashed line (right-hand axis) designates the solar incidence angle for the fixed-tilt microtracking panels. (c) Power generated per unit installed land area for each system; the dual axis panel spacing in this case is optimized to avoid shading for tilt angles up to 50°. As compared to (b), in this case the planar microtracking system generates nearly twice as much energy on aggregate as the dual axis system over a typical day since more microtracking panels can be located in a given land area without shading.

Chapter 3
Summary and Future Work

In this chapter, we provide supplemental discussion for the designs and simulations in Chapter 2. Future applications in the areas of high gain ($G \approx$1000x), rooftops or other limited space environments, and several defense-related areas are discussed.

3.1 Summary and Discussion

As compared to traditional Fresnel lens CPV systems, embedded microcell microtracking may hold several advantages, particularly for enabling CPV application in urban areas and on rooftops where orientation-based systems have been impractical. In addition to improved land use efficiency (cf. Figure 2.6), microtracking is expected to reduce susceptibility to wind load tracking error and simplify the overall support and tracking infrastructure. At approximately 1 cm thick, microtracking concentration is dramatically more compact than previous approaches to fixed panel CPV and the index-matched nature of the concentrator stack enables substantially higher optical efficiency. Because lateral displacement of the microcell sheet is limited to $\sim$1 cm (i.e. the lenslet pitch) and all movement interfaces are internal and protected, this approach should be mechanically robust, in many respects resembling fixed-panel PV more than traditional CPV.

Cost and scalability are also addressed. High efficiency microcells are now fabricated economically in releasable, multilayer stacks and transfer-printing has been demonstrated to pattern and connect them with sub-micron precision and high yield over large (Gen 2.5) areas. [44, 61] Recent cost analysis [71] and commercial success [37] for microcell CPV systems support the potential of this manufacturing approach to be cost-competitive in the photovoltaic marketplace. Simple modes of automated mechanical microtracking have already been demonstrated [57] and injection molding enables low cost, high throughput fabrication of plastic lenslet arrays using the same stabilizer additives as existing CPV Fresnel lenses to mitigate ultraviolet-induced yellowing. Mechanical weathering and soiling of the upper lenslet surface are an inevitable concern with plastic optics, though major surface damage could ultimately be resolved by sliding off and replacing the upper lenslet

array. While the detailed impact of thermal expansion and refractive index change arising from climatic variation remains to be investigated, initial estimates suggest a negligible change in focal length and spot size (<1%) over a 50 °C temperature swing whereas registration between the microcell and lenslet arrays should be maintained since both are constructed on/from the same plastic.

Taken together, our results demonstrate microcell microtracking as a viable route to combine the high efficiency and cost leverage of CPV with the siting versatility and operational robustness of fixed panel PV. Anti-reflection coatings applied to the upper lenslet and microcell surfaces are predicted to maintain full-day optical efficiency between 80% and 95% whereas global optimization of the lenslet surfaces and microcell size should further increase the concentration ratio. Supported by the development of multijunction tandem microcells with demonstrated efficiency exceeding 40%, [70, 72] the embedded microtracking approach described here may provide a new path for efficient, compact, and inexpensive photovoltaic power.

3.2 Future Work

Before concluding the thesis, we briefly outline potential future directions for this work, mainly higher levels of gain and applications to both locations where surface area is at a premium (i.e. cities or residential roofing installations) and the defense industry.

3.2.1 Towards Higher Gain

Virtually all PV cells with a power conversion efficiency >40% have used multijunction cells under concentration levels between 400-1000x. [35] The planar designs discussed earlier in this document have gains on the order of 255-260x; because these were proven to work, an obvious next step is to increase the gain by adjusting the lenslet-to-PV area ratio and optimizing the folded optical stack. Figure 3.1a shows such a design, where the focal spot has been significantly sharpened compared to that of 1.5c at the expense of angular acceptance ($G = 1395$ vs 450).

Figure 3.1b shows what happens to this design as it is aligned to a microcell of varying sizes, allowing for geometric gains from 500x up through 1018x. Although the range of incident angles is restricted to $\pm 50^\circ$ before the optical efficiency of the system drops below 60% (between 6-7 hours of operation per day), this configuration may still be economically justifiable given the small amount of sunlight sacrificed in the morning and late afternoon cf. Figure 2.6c.

3.2.2 Urban Environments and Land Area-Limited Applications

The results demonstrated thus far represent a significant step towards the goal of inexpensive, high efficiency embedded CPV systems that can be integrated on

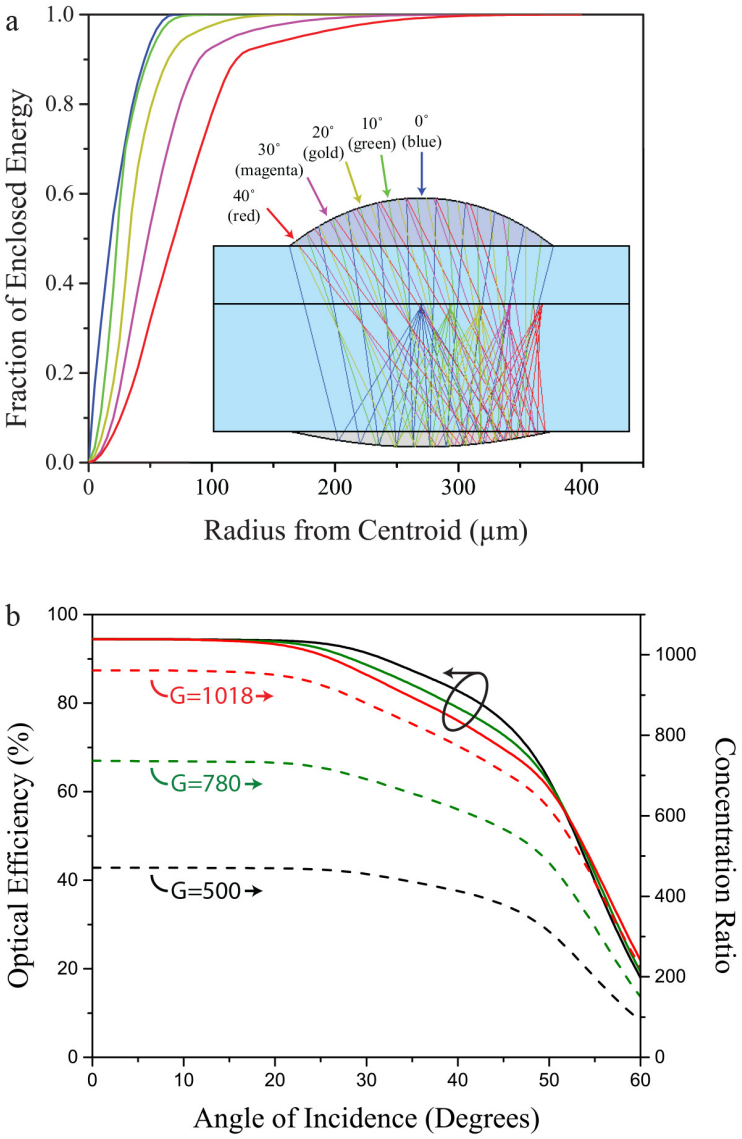

Figure 3.1. (a) Ray tracing analysis of an acrylic lenslet pairing optimized for high concentration ratio. The lenslet diameter (12.7 mm) is the same as in Figure 1.5c of the main text, however the greater asymmetry in curvature between the top and bottom lenslets here yields a significantly sharper focal spot, with >90% of the power in the focal plane lying within a 250 μm diameter spot for incidence angles up to 45°. The drawback to this design however, is that at higher incidence angles a portion of light refracted from the top lenslet falls outside of the bottom mirror (e.g. farther to the right in the inset) leading to decreased optical efficiency. (b) Simulation of the lenslet design in (a) extended to a hexagonally-tiled quasi-infinite array (analogous to that in Figure 2.1b of the main text) with square microcells of decreasing size yielding geometric gains G = 500, 780, and 1018. Optical efficiency >70% is maintained for all geometric gains up to 45° incidence, which corresponds to approximately 6 hours operation per day according to Figure 1.5d of the main text.

building rooftops and other limited-space urban environments in the form factor of standard fixed panel PV. As shading losses for our planar CPV design are significantly reduced when compared to other non-planar CPV, it is able to provide a much higher areal power density (see Figure 2.6c). Moreover, a typical large CPV module requires significantly more infrastructure, with foundation depths on the order of 5 m [75] which relegates them to large, open fields. In doing so, these consolidated CPV plants incur a ∼10% transmission loss to the electrical grid, thereby throwing away one of the potential advantages that PV has over nearly every other power source, most of which also require centralized facilities.

With all of this being noted, there is a tremendous amount of untapped area available on both residential and urban rooftops. It is already common to see static Si panels on top of peoples homes, and with the recent drop in cost of c-Si, modules with efficiencies near 18% [53] have become commercially available at reasonable prices. Knowing that fixed-panel PV requires minimal structural support or architectural modification to the edifice on which it is placed, this is the most common form of PV commanding the vast majority of the $\sim$ 20 GW_P [21] of global installed PV power generation capacity. To date, the several attempts to implement CPV in a compact, planar form factor [76, 77] have seen limited adoption; now, with the advent of microscale PV cells coupled to our folded optical design, rooftop CPV stands to become more of a reality.

The low profile of the planar microtracking CPV presented in this thesis gives it nominally the same form-factor and dimensions as fixed-plate PV. Though there is the added complexity of a tracking system and optics, this design is capable of generating ∼1.3X more power on both a panel-by-panel or areal basis when compared to an 18% efficient Si module. This is based off of the modest assumption of a 30% efficient microcell module. Modules of 4J microcells exceeding efficiencies of 36% have been demonstrated [44], and as multijunction PV technology continues to get better, CPV is expected to reap the benefits. Furthermore, other groups have also been working on microcell CPV systems with various configurations of optics, solar cell materials, and trackers. [44, 69, 70] Cost projection models indicate a high likelihood of being able to reduce the total system cost below \$1/W_P [71] by 2020.

3.2.3 Defense Applications

In order to decrease combat vulnerability, the Department of Defense (DoD) is looking to reduce the need and frequency of fuel and battery resupplies. The Naval Research Lab's (NRL's) most recent undertaking involved a compact, light weight, 19% efficient "solar blanket" which utilized flexible single junction GaAs solar cells fabricated via epitaxial liftoff. [73] Due to its modularity and scalability, it may be possible to design a light weight, flexible version of the planar concentrator presented in this thesis. To increase durability, all of the optical elements could be

fabricated out of PDMS, a flexible polymer which has reasonable optical qualities at visible wavelengths. With proper modifications to the transfer printing process used to place the PV elements, a flexible substrate may replace the thin glass presently in use. Finally, small linear actuators could be exploited to provide the necessary translation for tracking. Because the entire system is ∼1 cm thick, it could be constructed and stowed in a small box until it was needed, or individual components could be rolled up, transported, and assembled at a camp site.

Assuming PDMS has a density of 0.965 g/cm^2, and the dimensions of the concentrator were 26 x 39.4 x 0.9 cm^3, its total mass would be 890 g, or approximately 3x that of the thin film GaAs panels used by the NRL for their field test. As shown in 3.2.1, the system can be modified for higher gain through a series of global optimizations. If necessary, the thickness of the system could be scaled down while maintaining high gain as demonstrated above; doing so would further reduce the mass, yet sustain the high efficiency of this design. The addition of ∼40% efficient multijunction microcells [70, 72] may provide an avenue for mobile CPV exceeding 30% efficiency.

A second application involves small, lightweight unmanned aerial vehicles (UAVs) known as drones. There is a large effort under way to produce light weight power supplies for these air crafts; as with the solar blanket, many designs utilize thin-film GaAs cells for their high power-to-weight ratio, and Alta Devices has nearly managed to achieve 1 W/g. [74] Although the planar solar concentrator is below this power density, the PV substrate and spacer material may be able to perform as structural elements analogous to building-integrated CPV systems [52]. Additionally, if scaled to an appropriate size, it is possible that the optical elements may enhance aerodynamics. A fluid-mechanical model should be undertaken to better understand how this type of system might operate.

Appendix A
Methods

A.1 Optical Simulations in Zemax^{TM} and Comparison Between Tracking Designs

Non-sequential ray-tracing simulation was carried out using Zemax^{TM} optical modeling software accounting for all material absorption / optical constant dispersions and polarization-dependent Fresnel reflections. The geometry of the concentrator stack was simulated and optimized over the AM1.5D solar spectrum in the spectral band $400<\lambda<1100$ nm to enable implementation with either GaAs or multijunction microcells. In Figure 2.6, the power density of a given panel is calculated as

$$P_D(\theta_{inc}) = \eta_{cell}\eta_{opt}(\theta_{inc})I_{DNI}(\theta_{inc}) \tag{A.1}$$

where the net conversion efficiency of the module cell array was chosen to be η_{cell}=30% and the optical efficiency (η_{opt}) is the fraction of light incident on the concentrator that is transmitted to the cells (including the $\cos(\theta_{inc})$ projection loss for the fixed tilt panels).

The direct normal irradiance component of the solar spectrum (I_{DNI}) was used with an air mass correction to account for intensity changes throughout the day resulting from variation in optical path length through the atmosphere. [78] In Figure 2.6c, dual axis tracking panels were spaced for optimal power per unit land area such that shading was avoided for panel tilts up to 50° from the zenith, resulting in a land area increase of $[\cos(50°)]^{-1}$ ∼1.55x in the east-west direction relative to microtracking panels spaced adjacent to one another. Latitude-tilted standard Si photovoltaic panels where simulated assuming the AM1.5G solar spectrum, a module efficiency of 18%, incidence angle-dependent Fresnel reflection losses, and the same panel-to-panel spacing as the microtracking CPV system. The system comparisons are calculated for a cloudless day at the vernal equinox in State College, PA.

A.2 Manufacturing of GaAs Microcells and Printed Optics

Microcell photovoltaics were grown on GaAs substrates using metal-organic chemical vapor deposition (MOCVD). The cell structure (from bottom to top) includes: the GaAs substrate, a 500 nm $Al_{0.95}Ga_{0.05}As$ sacrificial layer, a 2000 nm p-GaAs (p = 3 x 10^{19} cm^{-3}) bottom contact layer, a 100 nm p-$Al_{0.3}Ga_{0.7}As$ (p = 5 x 10^{18} cm−3) back surface field layer, a 2000 nm p-GaAs (p = 1 x 10^{17} cm−3) base layer, a 100 nm n-GaAs (n = 2 x 10^{18} cm−3) emitter layer, a 30 nm n-$Al_{0.3}Ga_{0.7}As$ (n = 5 x 10^{18} cm−3) window layer, and a 200 nm n-GaAs (n = 1 x 10^{19} cm−3) top contact layer; electrical contacts consist of 10 nm Cr / 200 nm Au. The solar cells are lithographically patterned (size 0.7 mm x 0.7 mm), with the $Al_{0.95}Ga_{0.05}As$ sacrificial layer removed by a hydrofluoric acid (HF) based solution (ethanol:HF = 1.5:1 by volume). Individual solar cells are subsequently transfer printed onto glass substrates using 2 μm thick SU-8 as an adhesive with electrical interconnects consisting of 10 nm Cr / 20 nm Au / 1000 nm Cu / 20 nm Au. [72, 79]

The single cell concentrator stack (Figures 2.2 and 2.3) was constructed using uncoated 12.7 mm diameter BK7 plano-convex lenses (Thorlabs) with focal lengths $f = 15$ mm and $f = 30$ mm for the top and bottom, respectively. The microcells were printed on 1 mm thick glass and sandwiched between the two lenses using index matching fluid (Cargille Labs). The printed lenslet arrays were fabricated by LUXeXcel Inc. on 2 mm and 3 mm thick acrylic plastic sheets for the refractive and reflective elements, respectively. These sheet thicknesses are larger than optimal for the optical design but were necessary to avoid substrate bowing due to contraction of the printed acrylic "ink" upon ultraviolet curing. Details are provided in Figure B.4, Appendix B.

A.3 Concentrator Testing and Microcell Characterization

The microcell sheet position was controlled manually in all experiments using a pair of crossed translation stages. The entire concentrator/lateral control apparatus was mounted on a sliding track and illuminated from above in order to vary the illumination incidence angle. Measurements were conducted in steady state with a source-measure unit using a laser-driven Xenon lamp (Energetiq) for broadband, collimated illumination (divergence $< 0.5°$) and all-reflective optics to avoid chromatic aberration. Details of the testing arrangement are available in Figure B.1 in Appendix B. Due to the size of the required illumination area (10 cm^2) and our limited lamp power, the incident intensity is less than one sun equivalent. Linearity of the microcell photocurrent at high concentration was confirmed separately for

illumination intensity exceeding 100 suns (Figure B.3).

Appendix B
Supporting Data

This appendix contains supplemental data and figures for the singlet configuration, solar cell performance, array configuration, and a figure showing how macroscopic surface error produces significant aberrations in the printed optics.

B.1 Supplemental Graphics and Data for Singlet Design

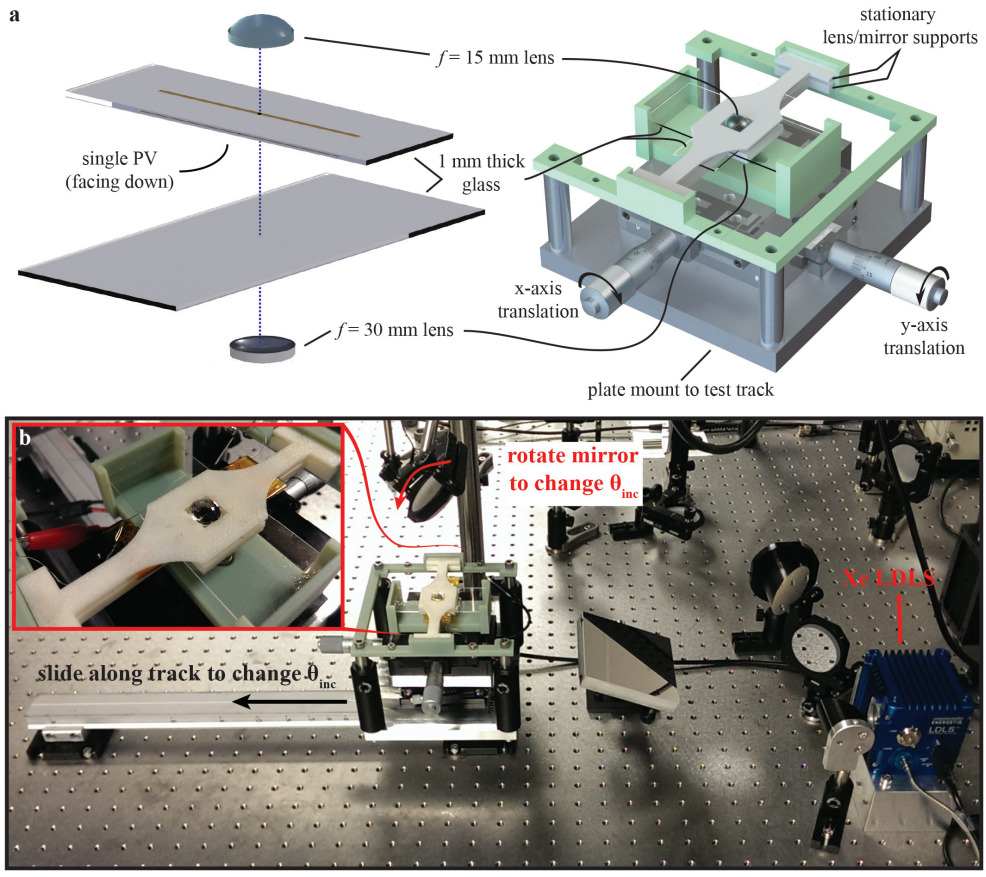

Figure B.1. (a) Exploded-view schematic of the single cell concentrator constructed using commercial off-the-shelf spherical plano-convex lenses. The microcell photovoltaic is transfer-printed and bonded facing down between 1 mm thick B270 glass slides using Norland optical adhesive (NOA 74) to eliminate any air gap. The upper refractive and lower reflective lenses have 12.7 mm outer diameter and focal lengths of 15 and 30 mm, respectively (Thorlabs parts LA1540 and LA1289, respectively); the reflective lens has a 150 nm thick coating of Ag applied to its convex surface. The glass/microcell center sheet is subsequently sandwiched between the lenses using index matching fluid (Cargille) and the entire assembly is held together in a 3-D printed test fixture shown at right using crossed translation stages to position the microcell relative to the stationary lenses. (b) Photograph of the indoor testing arrangement. Broadband light is collimated from a laser-driven Xe lamp (Energetiq) using an off-axis parabaloidal mirror (beam divergence estimated $<0.5°$) and directed to the concentrator from above. Incidence angle is varied between 0° and 60° by sliding the entire test fixture along a track; the inset shows a close up of the concentrator assembled in its test fixture.

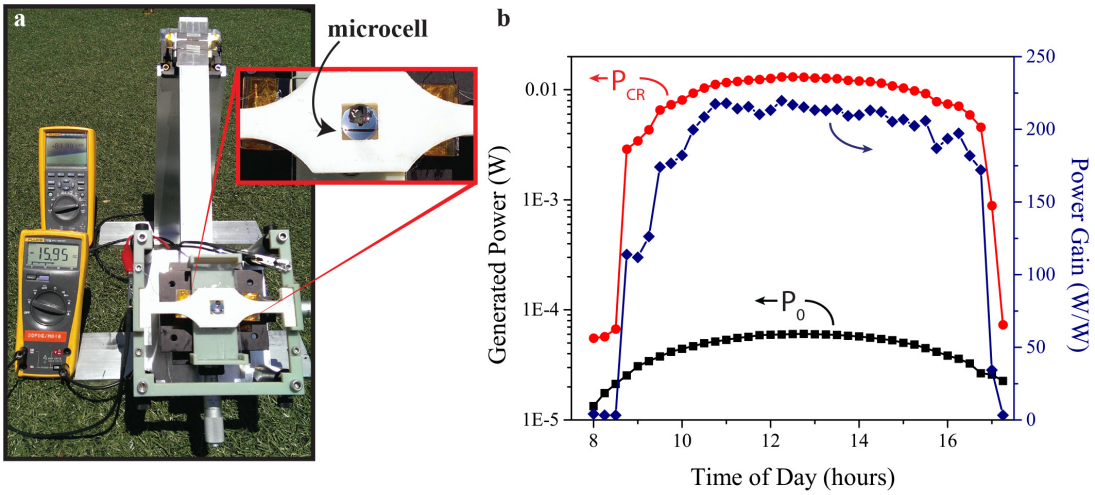

Figure B.2. (c) Photograph of the outdoor experimental configuration using the same test fixture as in B.1(b), tilted at 40.8° latitude. (d) Absolute maximum power output calculated for the day-long outdoor test in Figure 2.3a and 2.3b using short-circuit current and open-circuit voltage data recorded every 30 minutes and assuming a fill-factor of 0.78, invariant with incidence angle according to Figure 2.2d of the main text.

B.2 Solar Cell Performance Metrics Under Varying Levels of Concentration

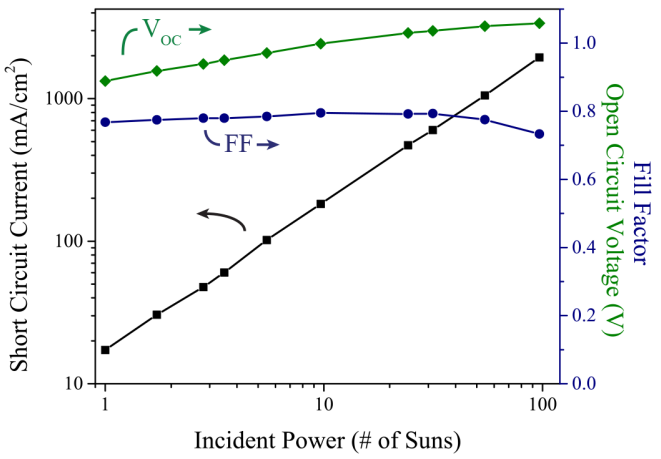

Figure B.3. Short-circuit current density (J_{sc}), open-circuit voltage (V_{oc}), and fill factor (FF) recorded as a function of AM1.5D simulated solar illumination intensity.

B.3 Supplemental Graphics and Data for Printed Array Design

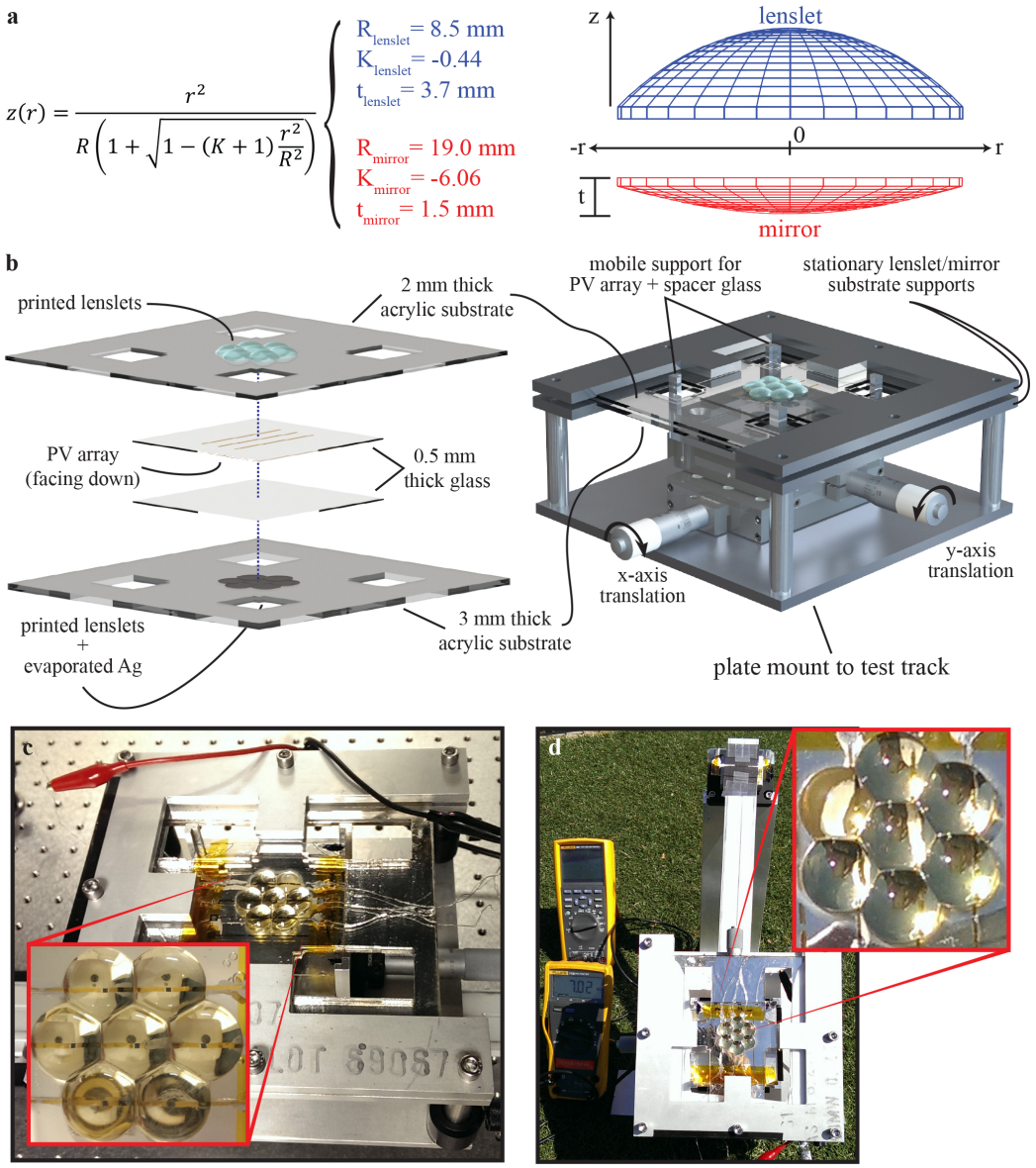

Figure B.4. (a) Wireframe diagram of a single printed lenslet (top, blue) and mirror (bottom, red). Each optic is characterized by its center thickness, t, and surface sag defined via the left-hand equation in terms of the radius of curvature, R, and conic constant, K. (b) Schematic of the inkjet printed, 7-element solar concentrator array assembled in the same manner as described in Supplementary Figure B.1a. The acrylic lenslet substrates in this case are purposely oversized, both to mitigate strain-induced bowing that occurs from curing in the printoptical process and to provide sufficient space for square through-holes that enable insertion of vertical corner brackets to control the position of the central glass/microcell array. (c) Photograph of the concentrator array assembled within the test fixture; the individual microcells can be seen as black squares in the inset close-up. (d) Photograph of the arrangement used for outdoor testing of the concentrator array.

B.4 A Comparison of Beam Quality After Passing Through Off-The-Shelf and Printed Optics

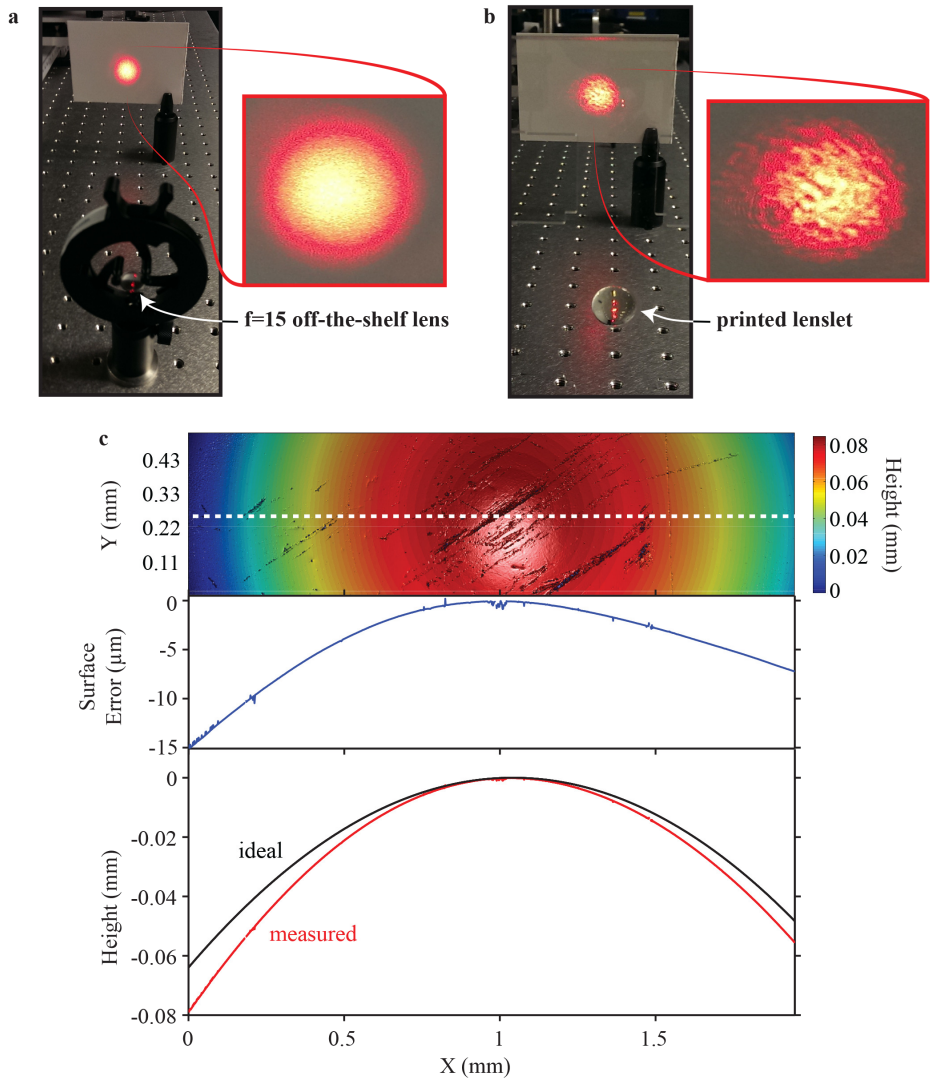

Figure B.5. (a) Photograph of a Gaussian HeNe laser beam focused by the 15 mm focal length commercial off-the-shelf plano-convex lens and expanded onto a white card. (b) The same laser projected through a single inkjet printed lenslet with similar focal length displays substantial deviation from a Gaussian profile, indicating the presence of large-scale lenslet surface error. (c) Surface profile measured for the printed lenslet shown in (b) using a Zygo New View 7300 optical profilometer. In addition to surface scratches, there is an approximate 20 deviation between the desired surface curvature (R = 8.5 mm, K = -0.44) and that extracted from a fit along the white dashed line (R 6.9, K 0) in the top profile image.

Bibliography

[1] (2014) *World Population Prospects: The 2012 Revision*, *report*, The United Nations.

[2] Moss, R. H., J. A. Edmonds, K. A. Hibbard, M. R. Manning, S. K. Rose, D. P. van Vuuren, T. R. Carter, S. Emori, M. Kainuma, T. Kram, G. A. Meehl, J. F. B. Mitchell, N. Nakicenovic, K. Riahi, S. J. Smith, R. J. Stouffer, A. M. Thomson, J. P. Weyant, and T. J. Wilbanks (2010) "The next generation of scenarios for climate change research and assessment," *Nature*, **463**(7282), pp. 747–756, 10.1038/nature08823.

[3] Pepper, W. J., R. J. Legget, R. J. Swart, J. Wasson, J. Edmonds, I. Mintzer, M. X. Wang, and J. Watson (1992) *Emission Scenarios for the IPCC An Update, Assumptions, Methodology, and Results*, *report*, United Stated Environmental Protection Agency.

[4] (2000) *Special Report on Emissions Scenarios*, *report*, Intergovernmental Panel on Climate Change.

[5] (2013) *Climate Change 2013: The Physical Science Basis*, *report*, Intergovernmental Panel on Climate Change.

[6] Thomson, A., K. Calvin, S. Smith, G. Kyle, A. Volke, P. Patel, S. Delgado-Arias, B. Bond-Lamberty, M. Wise, L. Clarke, and J. Edmonds (2011) "RCP4.5: a pathway for stabilization of radiative forcing by 2100," *Climatic Change*, **109**(1-2), pp. 77–94.

[7] Bureu, T. U. S. C. (2011), "2011 World Census," , Accessed: 2014-07-01.

[8] Bank, T. W. (2014), "GDP," , Accessed: 2014-07-01.

[9] (2013) *Key World Energy STATISTICS*, *report*, International Energy Agency.

[10] (2013) *CO_2 EMISSIONS FROM FUEL COMBUSTION*, *report*, International Energy Agency.

[11] Lewis, N. S. and D. G. Nocera (2006) "Powering the planet: Chemical challenges in solar energy utilization," *Proceedings of the National Academy of Sciences*, **103**(43), pp. 15729–15735.

[12] Wigley, T. M. L., R. Richels, and J. A. Edmonds (1996) "Economic and environmental choices in the stabilization of atmospheric CO_2 concentrations," *Nature*, **379**(6562), pp. 240–243.

[13] Maier-Reimer, E. and K. Hasselmann (1987) "Transport and storage of CO_2 in the ocean -an inorganic ocean-circulation carbon cycle model," *Climate Dynamics*, **2**(2), pp. 63–90.

[14] (2014) *Climate Change 2014: Mitigation of Climate Change, Summary for Policymakers*, *report*, Intergovernmental Panel on Climate Change.

[15] (2012) *Key World Energy STATISTICS*, *report*, International Energy Agency.

[16] (2005) *Carbon Dioxide Capture and Storage*, *report*, Intergovernmental Panel on Climate Change.

[17] (2003) *The Future of Nuclear Power, AN INTERDISCIPLINARY MIT STUDY*, *report*, Massachussets Institute of Technology.

[18] Deutch, J. e. a. (2009) *Update of the 2003 MIT Future of Nuclear Power, AN INTERDISCIPLINARY MIT STUDY*, *report*, Massachussets Institute of Technology.

[19] Hurricane, O. A., D. A. Callahan, D. T. Casey, P. M. Celliers, C. Cerjan, E. L. Dewald, T. R. Dittrich, T. Doppner, D. E. Hinkel, L. F. B. Hopkins, J. L. Kline, S. Le Pape, T. Ma, A. G. MacPhee, J. L. Milovich, A. Pak, H. S. Park, P. K. Patel, B. A. Remington, J. D. Salmonson, P. T. Springer, and R. Tommasini (2014) "Fuel gain exceeding unity in an inertially confined fusion implosion," *Nature*, **506**(7488), pp. 343–348.

[20] Lewis, N. S. (2007) "Powering the planet," *Mrs Bulletin*, **32**(10), pp. 808–820.

[21] Tao, M. (2014) *Terawatt Solar Photovoltaics: Roadblocks and Opportunities*, SpringerBriefs in Applied Sciences and Technology, 1 ed., Springer.

[22] Kalogirou, S. (2004) "Solar thermal collectors and applications," *PROGRESS IN ENERGY AND COMBUSTION SCIENCE*, **30**(3), pp. 231–295.

[23] Forristal, R. (2005) *Heat Transfer Analysis and Modeling of a Parabolic Trough Solar Receiver Implemented in Engineering Equation Solver*, *report*, National Renewable Energy Laboratory.

[24] Laboratory, N. R. E. (2010), "U.S. Parabolic Trough Power Plant Data," , url: $http://www.nrel.gov/csp/troughnet/power_plant_data.html$, Accessed: 2014-07-03.

[25] Green, M. A., K. Emery, Y. Hishikawa, W. Warta, and E. D. Dunlop (2014) "Solar cell efficiency tables (version 44)," *Progress in Photovoltaics: Research and Applications*, **22**(7), pp. 701–710.

[26] (2013) *Updated Capital Cost Estimates for Utility Scale Electricity Generating Plants*, *report*, U.S. Energy Information Administration.

[27] Shockley, W. and H. J. Queisser (1961) "Detailed Balance Limit of Efficiency of pâĂŘn Junction Solar Cells," *Journal of Applied Physics*, **32**(3), pp. 510–519.

[28] Nelson, J. (2003) *The Physics of Solar Cells*, Nelson Imperial College Press.

[29] Dong, H., L.-D. Sun, and C.-H. Yan (2013) "Basic understanding of the lanthanide related upconversion emissions," *Nanoscale*, **5**(13), pp. 5703–5714.

[30] Zou, W., C. Visser, J. A. Maduro, M. S. Pshenichnikov, and J. C. Hummelen (2012) "Broadband dye-sensitized upconversion of near-infrared light," *Nature Photonics*, **6**(8), pp. 560–564.

[31] Baluschev, S., V. Yakutkin, T. Miteva, G. Wegner, T. Roberts, G. Nelles, A. Yasuda, S. Chernov, S. Aleshchenkov, and A. Cheprakov (2008) "A general approach for non-coherently excited annihilation up-conversion: transforming the solar-spectrum," **10**.

[32] Deng, F., J. Blumhoff, and F. N. Castellano (2013) "Annihilation Limit of a Visible-to-UV Photon Upconversion Composition Ascertained from Transient Absorption Kinetics," *Journal of Physical Chemistry A*, **117**(21), pp. 4412–4419.

[33] Nozik, A. (2002) "Quantum dot solar cells," *PHYSICA E-LOW-DIMENSIONAL SYSTEMS & NANOSTRUCTURES*, **14**(1-2), pp. 115–120, 1st International Workshop on Nanostructures in Photovoltaics, MAX PLANCK INST PHYS KOMPLESER SYST, DRESDEN, GERMANY, JUL 28-AUG 04, 2001.

[34] Nozik, A. J., M. C. Beard, J. M. Luther, M. Law, R. J. Ellingson, and J. C. Johnson (2010) "Semiconductor Quantum Dots and Quantum Dot Arrays and Applications of Multiple Exciton Generation to Third-Generation Photovoltaic Solar Cells," *CHEMICAL REVIEWS*, **110**(11), pp. 6873–6890.

[35] (2014), "Best Research-Cell Efficiencies," , url: *http //www.nrel.gov/ncpv/images/efficiency_chart.jpg*, Accessed: 2014-06-30.

[36] Kurtz, S. (2012) *Opportunities and Challenges for Development of a Mature Concetrating Photovoltaic Power Industry, Report*, National Renewable Energy Laboratory.

[37] Semprius (2013), "Semprius 35.5 Percent Efficiency Sets New Record for Commercially Available Solar Modules," .

[38] Soitec (2014), "36.7 Percent for New Solar Module Using Highly Efficient Multi-Junction Solar Cells," .

[39] Chaves, J. (2008) *Introduction to Nonimaging Optics*, Optical science and engineering series, CRC Press.

[40] Xie, W. T., Y. J. Dai, R. Z. Wang, and K. Sumathy (2011) "Concentrated solar energy applications using Fresnel lenses: A review," *Renewable & Sustainable Energy Reviews*, **15**(6), pp. 2588–2606.

[41] Buljan, M., J. Mendes-Lopes, P. Benitez, and J. Carlos Minano (2014) "Recent trends in concentrated photovoltaics concentrators' architecture," *JOURNAL OF PHOTONICS FOR ENERGY*, **4**.

[42] Miller, D. C. and S. R. Kurtz (2011) "Durability of Fresnel lenses: A review specific to the concentrating photovoltaic application," *SOLAR ENERGY MATERIALS AND SOLAR CELLS*, **95**(8, SI), pp. 2037–2068.

[43] Baig, H., K. C. Heasman, and T. K. Mallick (2012) "Non-uniform illumination in concentrating solar cells," *Renewable & Sustainable Energy Reviews*, **16**(8), pp. 5890–5909.

[44] Sheng, X., C. A. Bower, S. Bonafede, J. W. Wilson, B. Fisher, M. Meitl, H. Yuen, S. Wang, L. Shen, A. R. Banks, C. J. Corcoran, R. G. Nuzzo, S. Burroughs, and J. A. Rogers (2014) "Printing-based assembly of quadruple-junction four-terminal microscale solar cells and their use in high-efficiency modules," *Nat Mater*, **13**(6), pp. 593–598.

[45] Zamora, P., P. Benitez, Y. Li, J. C. Minano, J. Mendes-Lopes, and K. Araki (2012) "The Dome-Shaped Fresnel-Kohler Concentrator," in *8TH INTERNATIONAL CONFERENCE ON CONCENTRATING PHOTOVOLTAIC SYSTEMS (CPV-8)* (Dimroth, F and Rubio, F and Anton, I, ed.), vol. 1477 of *AIP Conference Proceedings*, pp. 69–72, 8th International Conference on Concentrating Photovoltaic Systems (CPV), Toledo, SPAIN, APR 16-18, 2012.

[46] Benítez, P., J. C. M. nano, P. Zamora, R. Mohedano, A. Cvetkovic, M. Buljan, J. Chaves, and M. Hernández (2010) "High performance Fresnel-based photovoltaic concentrator," *Opt. Express*, **18**(S1), pp. A25–A40.

[47] Butel, G. P., B. M. Coughenour, H. A. Macleod, C. E. Kennedy, and J. R. P. Angel (2012) "Reflectance optimization of second-surface silvered glass mirrors for concentrating solar power and concentrating photovoltaics application," *JOURNAL OF PHOTONICS FOR ENERGY*, **2**(4).

[48] Chong, K.-K., S.-L. Lau, T.-K. Yew, and P. C.-L. Tan (2013) "Design and development in optics of concentrator photovoltaic system," *RENEWABLE & SUSTAINABLE ENERGY REVIEWS*, **19**, pp. 598–612.

[49] Coughenour, B. M., T. Stalcup, B. Wheelwright, A. Geary, K. Hammer, and R. Angel (2014) "Dish-based high concentration PV system with Köhler optics," *Optics Express*, **22**(S2), pp. A211–A224.

[50] Benitez, P., J. C. Minano, J. Blen, R. Mohedano, J. Chaves, O. Dross, M. Hernandez, and W. Falicoff (2004) "Simultaneous multiple surface optical design method in three dimensions," *Optical Engineering*, **43**(7), pp. 1489–1502.

[51] Vasylyev, S. V., V. P. Vasylyev, and V. A. Sergeev (2010) "Concept and design of "flat-plate" CPV module based on Ring-Array Concentrator," in *Photovoltaic Specialists Conference (PVSC), 2010 35th IEEE*, pp. 003087–003091.

[52] Chemisana, D. (2011) "Building Integrated Concentrating Photovoltaics: A review," *Renewable & Sustainable Energy Reviews*, **15**(1), pp. 603–611.

[53] Wang, X., J. Byrne, L. Kurdgelashvili, and A. Barnett (2012) "High efficiency photovoltaics: on the way to becoming a major electricity source," *Wiley Interdisciplinary Reviews: Energy and Environment*, **1**(2), pp. 132–151.

[54] Cumpston, J. and J. Pye (2014) "Shading and land use in regularly-spaced sun-tracking collectors," *Solar Energy*, **108**(0), pp. 199 – 209.

[55] Duerr, F., Y. Meuret, and H. Thienpont (2011) "Tracking integration in concentrating photovoltaics using laterally moving optics," *Optics Express*, **19**(10), pp. A207–A218.

[56] ——— (2013) "Tailored free-form optics with movement to integrate tracking in concentrating photovoltaics," *Optics Express*, **21**(9), pp. A401–A411.

[57] Hallas, J. M., K. A. Baker, J. H. Karp, E. J. Tremblay, and J. E. Ford (2012) "Two-axis solar tracking accomplished through small lateral translations," *Applied Optics*, **51**(25), pp. 6117–6124.

[58] Karp, J. H., E. J. Tremblay, and J. E. Ford (2010) "Planar micro-optic solar concentrator," *Optics Express*, **18**(2), pp. 1122–1133.

[59] Katz, E., J. Gordon, and D. Feuermann (2006) "Effects of ultra-high flux and intensity distribution in multi-junction solar cells," *PROGRESS IN PHOTOVOLTAICS*, **14**(4), pp. 297–303.

[60] Katz, E. A., J. M. Gordon, W. Tassew, and D. Feuermann (2006) "Photovoltaic characterization of concentrator solar cells by localized irradiation," *JOURNAL OF APPLIED PHYSICS*, **100**(4).

[61] Yoon, J., S. Jo, I. S. Chun, I. Jung, H.-S. Kim, M. Meitl, E. Menard, X. Li, J. J. Coleman, U. Paik, and J. A. Rogers (2010) "GaAs photovoltaics and optoelectronics using releasable multilayer epitaxial assemblies," *Nature*, **465**(7296), pp. 329–333, 10.1038/nature09054.

[62] Lee, J., J. Wu, J. H. Ryu, Z. J. Liu, M. Meitl, Y. W. Zhang, Y. G. Huang, and J. A. Rogers (2012) "Stretchable Semiconductor Technologies with High Areal Coverages and Strain-Limiting Behavior: Demonstration in High-Efficiency Dual-Junction GaInP/GaAs Photovoltaics," *Small*, **8**(12), pp. 1851–1856.

[63] Hecht, E. (2002) *Optics*, 4 ed., Pearson Education, Inc.

[64] Reda, A., I.; Andreas (2003) *Solar Position Algorithm for Solar Radiation Applications*, *Report NREL Report No TP-560-34302*, National Renewable Energy Laboratory.

[65] Mironov, V., R. P. Visconti, V. Kasyanov, G. Forgacs, C. J. Drake, and R. R. Markwald (2009) "Organ printing: Tissue spheroids as building blocks," *Biomaterials*, **30**(12), pp. 2164–2174.

[66] Choi, J.-W., H.-C. Kim, and R. Wicker (2011) "Multi-material stereolithography," *Journal of Materials Processing Technology*, **211**(3), pp. 318–328.

[67] (2012), "Additive Manufacture of Optics Goes Digital," .

[68] Küchel, M. F. (2009) "Interferometric measurement of rotationally symmetric aspheric surfaces," vol. 7389, pp. 16–34.

[69] Jared, B. H., M. P. Saavedra, B. J. Anderson, R. S. Goeke, W. C. Sweatt, G. N. Nielson, M. Okandan, B. Elisberg, D. Snively, J. Duncan, T. Gu, G. Agrawal, and M. W. Haney (2014) "Micro-concentrators for a microsystems-enabled photovoltaic system," *Optics Express*, **22**(S2), pp. A521–A527.

[70] Fidaner, O., F. A. Suarez, M. Wiemer, V. A. Sabnis, T. Asano, A. Itou, D. Inoue, N. Hayashi, H. Arase, A. Matsushita, and T. Nakagawa (2014) "High efficiency micro solar cells integrated with lens array," *Applied Physics Letters*, **104**(10), pp. –.

[71] Paap, S., V. Gupta, J. L. Cruz-Campa, M. Okandan, W. Sweatt, B. Jared, B. Anderson, G. Nielson, A. Tauke-Pedretti, and J. Nelson (2013) "Cost Analysis for Flat-Plate Concentrators Employing Microscale Photovoltaic Cells," in *2013 IEEE 39TH PHOTOVOLTAIC SPECIALISTS CONFERENCE (PVSC)*, IEEE Photovoltaic Specialists Conference, pp. 3431–3434, 39th IEEE Photovoltaic Specialists Conference (PVSC), Tampa, FL, JUN 16-21, 2013.

[72] Sheng, X., C. J. Corcoran, J. He, L. Shen, S. Kim, J. Park, R. G. Nuzzo, and J. A. Rogers (2013) "Enhanced ultraviolet responses in thin-film InGaP solar cells by down-shifting," *Physical Chemistry Chemical Physics*, **15**(47), pp. 20434–20437.

[73] Trautz, K. M., P. P. Jenkins, R. J. Walters, D. Scheiman, R. Hoheisel, R. Tatavarti, R. Chan, H. Miyamoto, J. G. J. Adams, V. C. Elarde, and J. Grimsley (2013) "Mobile Solar Power," *IEEE JOURNAL OF PHOTOVOLTAICS*, **3**(1), pp. 535–541.

[74] AltaDevices (2013), "Application Brief: Solar Powered Unmanned Systems," .

[75] Arzon Solar, http://arzonsolar.com/amonix-8700-solar-power-generator/ Accessed: 2014-10-20.

[76] Zettasun, Inc., http://www.zettasun.com/ Accessed: 2014-10-20.

[77] SunCycle, http://suncycle.nl/ Accessed: 2014-10-20.

[78] Kasten, F. and A. T. Young (1989) "REVISED OPTICAL AIR-MASS TABLES AND APPROXIMATION FORMULA," *Applied Optics*, **28**(22), pp. 4735–4738.

[79] Sheng, X., L. Shen, T. Kim, L. Li, X. Wang, R. Dowdy, P. Froeter, K. Shigeta, X. Li, R. G. Nuzzo, N. C. Giebink, and J. A. Rogers (2013) "Doubling the Power Output of Bifacial Thin-Film GaAs Solar Cells by Embedding Them in Luminescent Waveguides," *Advanced Energy Materials*, **3**(8), pp. 991–996.